J. Fluid Mech. (1989), *vol.* 207, *pp.* 153–189
Printed in Great Britain

Time-dependent convection in a fluid-saturated porous cube heated from below

By S. KIMURA[1], G. SCHUBERT[2] AND J. M. STRAUS[3]

[1] Government Industrial Research Institute, Tohoku-Nigatake 4-2-1, Sendai 983, Japan

[2] Department of Earth and Space Sciences, University of California, Los Angeles, CA 90024-1567, USA

[3] Laboratory Operations, The Aerospace Corporation, PO Box 92957, Los Angeles, CA 90009, USA

(Received 7 December 1987 and in revised form 2 March 1989)

A numerical scheme based on the pseudospectral method has been implemented in order to study three-dimensional convection in a fluid-saturated cube of porous material. With increasing Rayleigh number R, convection first evolves from a symmetric steady state (S) to a partially non-symmetric steady state (S′, physical symmetry in the vertical direction is preserved). The transition Rayleigh number is about 550. At a Rayleigh number of 575 the flow becomes oscillatory $P^{(1)}$ with a single frequency that increases with R. At a value of R between 650 and 680 the oscillation becomes quasi-periodic with at least two fundamental frequencies. It returns to a simply periodic state in a narrow range about $R = 725$. A further increase of R transforms the simply periodic state again to a quasi-periodic state. The sequence of three-dimensional time-dependent states resembles previously studied two-dimensional cases in that evolution from more complex states to less complex states occurs with increasing R. The partial symmetry breaking prior to the onset of time dependence is unique to the three-dimensional flows, but a dependence of the $S \rightarrow S'$ transition on the step size in R suggests the possibility that $S \rightarrow S'$ might not occur prior to $S \rightarrow P^{(1)}$ for sufficiently small steps in R. The quasi-periodic flows sometimes exhibit intermittency, causing difficulty in exactly defining their spectral characteristics.

1. Introduction

Strictly three-dimensional convection in a cube of fluid-saturated porous material occurs when the Rayleigh number R exceeds $4.5\pi^2$ (Beck 1972). Hereafter we shall refer to this three-dimensional convection as (1, 1, 1); it involves coupled disturbances in all three orthogonal directions. (Steen 1983 has shown that (1, 1, 1) convection is unstable in the range $4.5\pi^2 < R < 4.87\pi^2$.) The stable (1, 1, 1) convection is fundamentally different from three-dimensional convection formed by the superposition of two horizontal orthogonal rolls (Zebib & Kassoy 1978). One of the earliest attempts to investigate the nonlinear regime in a cube was made by Holst & Aziz (1972) who carried out numerical computations for $R = 60$ and 120. Horne (1979) has also obtained solutions up to $R = 400$ by using finite differences. Straus & Schubert (1979) used the Galerkin technique to study steady convection in a cube for R up to 150, and later extended the calculations for Rayleigh numbers up to 500 (Schubert & Straus 1979). Both Schubert & Straus (1979) and Horne (1979) found that the flows are oscillatory at sufficiently high Rayleigh number ($R > 300$).

Fluctuating porous-medium thermal convection was first discovered by Horne & O'Sullivan (1974) for a unicellular mode in two dimensions; the existence of this fluctuating state was confirmed by Caltagirone (1975) and Schubert & Straus (1979). Other workers also reported the presence of time dependence in porous-medium thermal convection (Gary & Kassoy 1981; Gary *et al.* 1982). However, the critical Rayleigh number reported by the various investigators for the onset of oscillation in a square cell has varied. For example, the critical value determined by Horne & O'Sullivan (1974) was $R = 280$, while Caltagirone (1975) found $R = 384 \pm 5$. The definitive value of this critical Rayleigh number has been established only recently as $R = 390$ by Kimura, Schubert & Straus (1987) and Aidun & Steen (1986, 1987).

Characterization of post-critical behaviour of two-dimensional convection was first studied by Schubert & Straus (1982) with the Galerkin method. They reported that the time-dependent solution evolves from a simply periodic state ($P^{(1)}$) to a quasi-periodic state (QP_2) with two independent frequencies. A further increase of the Rayleigh number transforms the QP_2 state to another simply periodic state ($P^{(2)}$). The work has been extended by Kimura, Schubert & Straus (1986, 1987), who have employed a pseudospectral method (Orszag 1971; Gottlieb & Orszag 1977). In their computations non-symmetric spectral coefficients, which were neglected in the work of Schubert & Straus (1982), were included and much higher truncation numbers ($N \leqslant 56$) were used. Kimura *et al.* (1986, 1987), identified the route to chaotic convection for the two-dimensional square-cell mode as

$$S \rightarrow P^{(1)} \rightarrow QP_2^{(1)} \rightarrow P^{(2)} \rightarrow QP_2^{(2)} \rightarrow P^{(3)} \rightarrow NP,$$

where S and NP denote steady and non-periodic states, respectively. The transition from $P^{(3)}$ to NP takes place at a Rayleigh number somewhere between 850 and 1000. The calculations have been performed up to $R = 1200$.

The sequence of transitions leading to the NP state is similar to that observed in Hele-Shaw convection (Koster & Müller 1984). It is, however, different from experimental observations with Newtonian fluids (Gollub & Benson 1980) in which the bifurcations have been found to always take place towards more complex time-dependent flows. In the course of numerical computations Kimura *et al.* (1986) as well as Schubert & Straus (1982) demonstrated that the time-dependent solutions are very sensitive to truncation of the spectral representation: over-truncation often leads to spurious transitions (Marcus 1981). Great care is particularly needed in order to characterize time-dependent solutions.

The present work is an extension of the work of Schubert & Straus (1982) and Kimura *et al.* (1986) and aims at characterization of time-dependent solutions in a three-dimensional space (a cube). As already mentioned, studies of three-dimensional thermal convection in porous media have been very limited. Probably the first calculations finding fluctuating convection in three dimensions were made independently by Schubert & Straus (1979) and Horne (1979). By invoking certain symmetry conditions for realizable flows (symmetry about two diagonals at each horizontal cross-section and antisymmetry with respect to the midheight horizontal plane and a 90° rotation about $\xi = \eta = 0.5$; see figure 1), Schubert & Straus (1979) found that convection in a cube evolves from steady to simply periodic at $R = 330$, and at $R = 400$ it transitions to more complex fluctuations. On the other hand, Horne (1979), who used a finite-difference scheme on a $17 \times 17 \times 17$ mesh, found that the symmetry conditions about diagonals on each horizontal cross-section were already violated for steady-state solutions at $R = 300$. His results are intriguing, because it implies that the symmetry conditions hypothesized by Schubert & Straus

(1979) may not be guaranteed at arbitrarily high Rayleigh numbers. Although neither investigation reported the nature of the time-dependent solutions in detail, the results showed that, in general, the frequencies and the amplitudes in the Nusselt-number variations tend to increase with the Rayleigh number.

For the present study we have generalized the algorithms of our previous work (Kimura *et al.* 1986) to apply to three dimensions. We shall not impose any *a priori* symmetry conditions on the solutions. In the next section we briefly describe the mathematical formulation and the numerical procedure. We then present numerical results for the evolution with R (up to $R = 740$) of three-dimensional thermal convection in a cube of fluid-saturated porous material.

2. Mathematical formulation and numerical procedure

The mathematical formulation in the present study is identical to that in Straus & Schubert (1979) and Schubert & Straus (1979). Therefore, only a brief description will be provided in this section. We assume the validity of Darcy's law, the Boussinesq approximation and thermal equilibrium between the fluid and the porous matrix. The vanishing of vertical vorticity under these assumptions allows the introduction of a potential ϕ whose second derivatives yield the Darcy velocity components

$$u = \phi_{\zeta\xi}, \quad v = \phi_{\zeta\eta}, \quad w = -(\phi_{\xi\xi} + \phi_{\eta\eta}), \tag{1}$$

where u, v and w are the non-dimensional Darcy velocity components in the non-dimensional ξ-, η- and ζ-coordinate directions, respectively, as shown in figure 1. It is then possible to derive a single governing equation for ϕ:

$$\frac{\partial}{\partial\tau}\nabla^2\phi + \phi_{\xi\zeta}\nabla^2\phi_\xi + \phi_{\eta\zeta}\nabla^2\phi_\eta - (\phi_{\xi\xi} + \phi_{\eta\eta})\nabla^2\phi_\zeta = \nabla^4\phi + R(\phi_{\xi\xi} + \phi_{\eta\eta}), \tag{2}$$

where τ is dimensionless time. The non-dimensional temperature θ is related to ϕ according to

$$\theta = -\frac{1}{R}\nabla^2\phi. \tag{3}$$

Aforementioned non-dimensional quantities are defined by

$$\left.\begin{aligned} (\xi, \eta, \zeta) &= \frac{(x, y, z)}{d}, \quad \tau = \frac{kt}{\chi d^2}, \\ (u, v, w) &= \frac{\rho c d}{k}(u_*, v_*, w_*), \\ \theta &= \frac{T - T_0 - \Delta T(1-\zeta)}{\Delta T}, \end{aligned}\right\} \tag{4}$$

where asterisks in the velocity components denote dimensional quantities, d is the height of the cube, k is the effective thermal conductivity, χ is the volume-averaged thermal capacity of the porous matrix and the saturated fluid, ρ is the fluid density, c is the specific heat of the fluid, T_0 is the top surface temperature and $T_0 + \Delta T$ is the temperature of the bottom surface. The Rayleigh number is defined as

$$R = \frac{\alpha g \rho^2 K \Delta T d}{\mu k}, \tag{5}$$

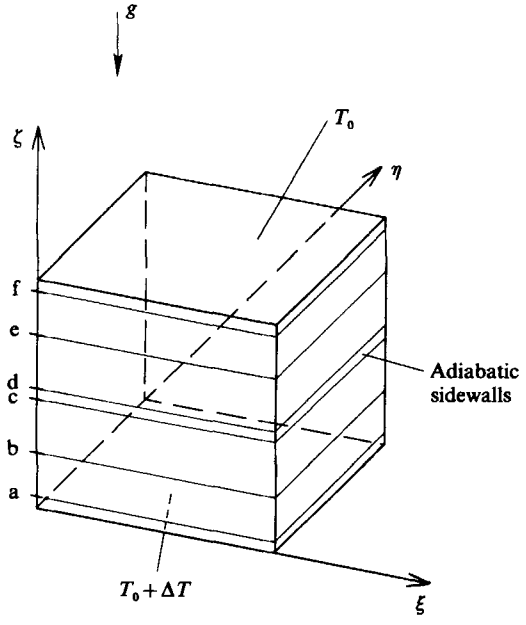

FIGURE 1. Schematic diagram of saturated, porous cube heated from below and the coordinate system. The vertical positions of horizontal cuts are shown by a–f. Numerical values of ζ corresponding to a–f vary depending on the truncation number N and they are tabulated in table 1.

where α is the thermal expansion coefficient of the fluid, μ is the fluid viscosity, g is the gravitational acceleration and K is the permeability of the porous matrix.

The boundary conditions on ϕ are

$$\left.\begin{aligned} \phi_{\xi\xi}+\phi_{\eta\eta}=\phi_{\zeta\zeta}=0 \quad &\text{on} \quad \zeta=0,1, \\ \phi_{\xi\xi}=\nabla^2\phi_\xi=0 \quad &\text{on} \quad \xi=0,1, \\ \phi_{\eta\zeta}=\nabla^2\phi_\eta= \quad &\text{on} \quad \eta=0,1. \end{aligned}\right\} \tag{6}$$

Physically, (6) states that the sidewalls are thermally insulating, the horizontal surfaces are isothermal, and all walls are impermeable.

Following Straus & Schubert (1979), the Galerkin representation for ϕ, which satisfies all the boundary conditions term by term, is

$$\phi(\tau,\xi,\eta,\zeta)=\sum_{n=1}^{\infty}\sum_{j=0}^{\infty}\sum_{m=0}^{\infty}\Phi_{njm}(\tau)\sin(n\pi\zeta)\cos(j\pi\xi)\cos(m\pi\eta). \tag{7}$$

Substitution of (7) into (2) and use of the orthogonality relations among the trigonometric functions yields an infinite set of coupled, nonlinear, first-order ordinary differential equations for the $\Phi_{njm}(\tau)$. These equations are truncated diagonally, such that the sum of n, j and m does not exceed a specified positive integer N, the truncation number.

Characterization of the time-dependent solution is made by monitoring the Nusselt number defined by

$$Nu(\tau)=\frac{q}{k\Delta T/d}=1-\sum_{n=1}^{\infty}\frac{n^3\pi^3}{R}\Phi_{n00}(\tau) \tag{8}$$

where q is the horizontally averaged heat flux. The Nusselt number is a suitable parameter for testing the accuracy of the numerical results. It has been found by

Straus & Schubert (1979) that three-dimensional flows require more terms to achieve a given accuracy than does two-dimensional convection. For example they reported that for $100 < R < 150$, $N = 10$ is necessary for Nu to be accurate to within 1%, while Straus (1974) found that $N = 6$ was adequate to give Nu to the same accuracy for two-dimensional flows with R as large as 150.

The set of coupled nonlinear equations for Φ_{njm} are solved numerically by the pseudospectral method (Orszag 1971; Gottlieb & Orszag 1977). The basic idea of the method is to evaluate the nonlinear products in physical space by transforming each factor of a nonlinear term from spectral space to physical space with the fast Fourier transform (FFT). The evaluated nonlinear products are then decomposed into spectral components by the inverse FFT. Since the number of spectral coefficients for a given truncation number N is proportional to N^3 in three-dimensional convection, overall computation time for the nonlinear products in spectral space would be proportional to N^6. On the other hand, the number of manipulations needed for nonlinear products in physical space is merely proportional to N. This implies a significant reduction in the amount of computing time, particularly for large truncation numbers.

Considerable care is required with the FFT to reduce aliasing errors. The diagonal truncation (i.e. $n+j+m \leqslant N$) prevents simultaneous aliasing from more than one spatial direction. Comparisons of pseudospectral and Galerkin solutions indicate that diagonal truncation significantly reduces aliasing effects on both time-averaged and time-dependent quantities. We further reduced the effects of aliasing by adding zeros to the truncated set of spectral coefficients before taking the inverse FFT. The results of this procedure will be discussed in the following section.

In a series of three-dimensional computations based on the Galerkin method, Straus & Schubert (1979) and Schubert & Straus (1979) enforced various symmetry conditions on the spectral coefficients (viz. that the sum of any pair of n, m and j be even). This enforces symmetry about horizontal diagonals and antisymmetry with respect to a reflection about the midplane $\zeta = 0.5$ and a rotation of 90° about the line $\xi = \eta = 0.5$; it reduces the *a priori* non-zero spectral coefficients from 220 to 55 for $N = 10$, for example. In the calculations presented here, we have relaxed these symmetry restrictions, and have included the complete set of spectral coefficients in the numerical computations (as long as they satisfy the diagonal truncation). This enables us to study the more general properties of convection in a cube.

In figure 2 we show the computational speed measured on the IBM3090 as a function of N. The ordinate indicates actual CPU time (s) required to yield spectral coefficients at a new time $\Phi_{njm}(\tau+\Delta\tau)$ from the previous values $\Phi_{njm}(\tau)$. At low truncation numbers the speeds of both methods are comparable, while the pseudospectral code is faster than the Galerkin code if the truncation number exceeds $N = 8$. Since the computation time for the pseudo-spectral code and the Galerkin code increase as N^3 and N^6 respectively, the former is significantly more efficient than the latter at large truncation numbers. For example, at $N = 100$ the present code would be approximately 1000 times faster than the Galerkin code. In the range of typical truncation numbers employed in the present study, the pseudospectral code runs roughly 100 times faster than the Galerkin code. The calculations reported here were partly carried out on the CRAY-XMP using single precision; however most of the computations were done on the IBM3081K with double precision; both computers use 14 significant figures.

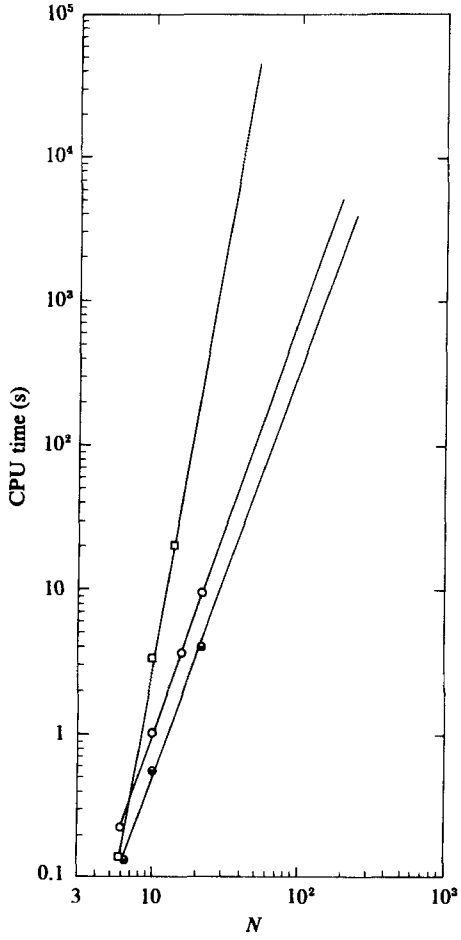

FIGURE 2. Respective computing speeds of the Galerkin code (□) and the pseudospectral code (○, ◒) on an IBM3090 as a function of truncation number N. The computing speed of the pseudospectral method is dependent on the FFT subroutine called within the code; use of the FFT in the ESSL subroutine package (◒) makes the code about twice as fast as that of the FFT in the IMSL package (○). The plotted CPU time is the actual computing time required to advance a specified $\Delta\tau$.

3. Discussion of results

3.1. *Symmetric steady-state convection*: S

We started our numerical computations by setting a large value for the spectral coefficient Φ_{111}. For Rayleigh numbers 80, 120 and 150 we confirmed that the present code generates identical results to those reported in Straus & Schubert (1979). The computations were continued to larger values of the Rayleigh number with truncation numbers N as large as 26. We found that the symmetries assumed by Straus & Schubert (1979) were valid up to $R = 500$. Representative isotherms and flow patterns in horizontal planes are shown in figure 3 for $R = 250$. The vertical positions of the planes (a–f) are illustrated in figure 1 and given in table 1. Contours of constant ϕ in figure 3(a) indicate deviations of the temperature from the conductive state. Hot spots at diagonally facing corners gradually expand as the fluid ascends, and at $\zeta = 0.5$ the ascending hot region occupies half of the cross-

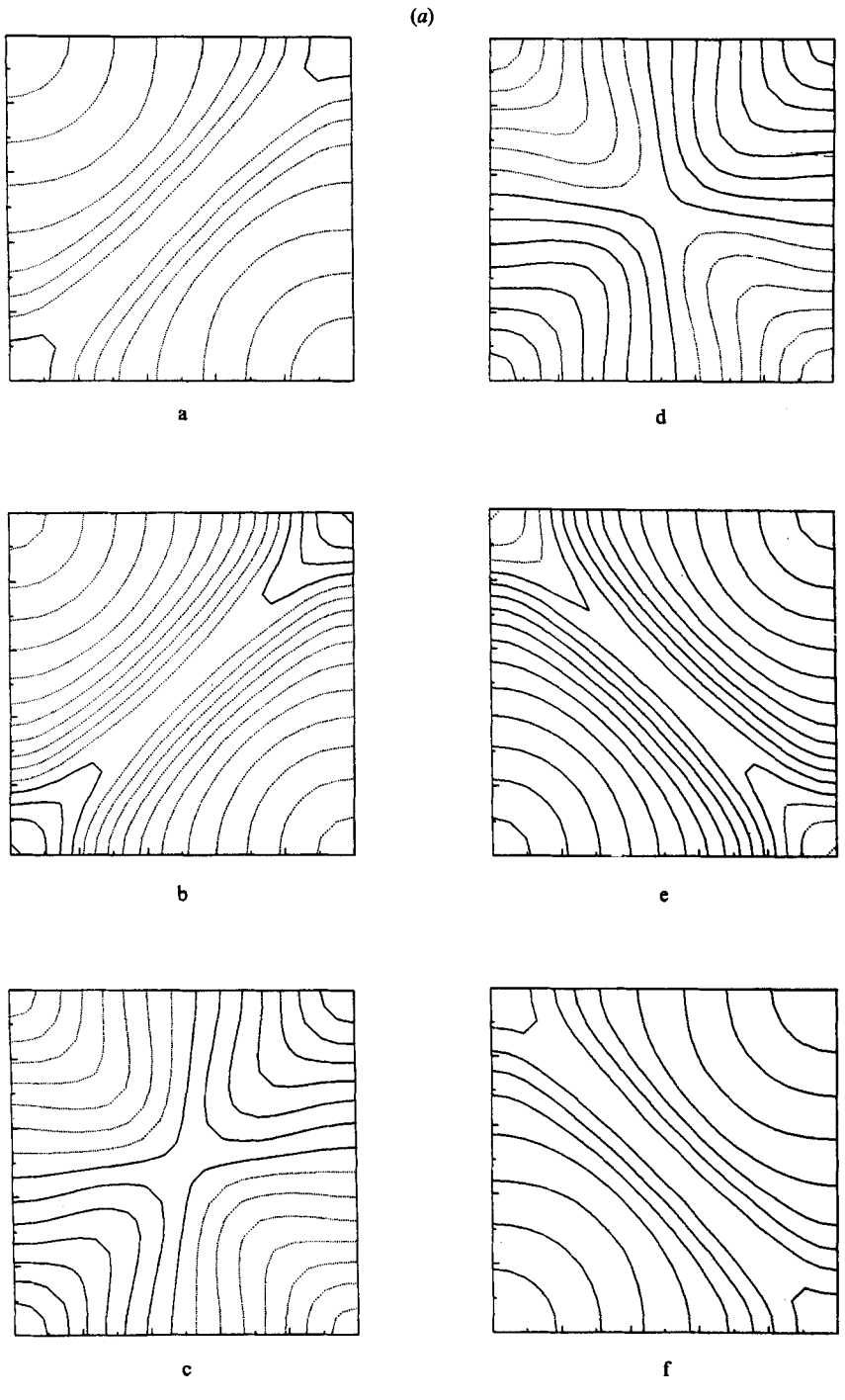

FIGURE 3(*a*). For caption see page 161.

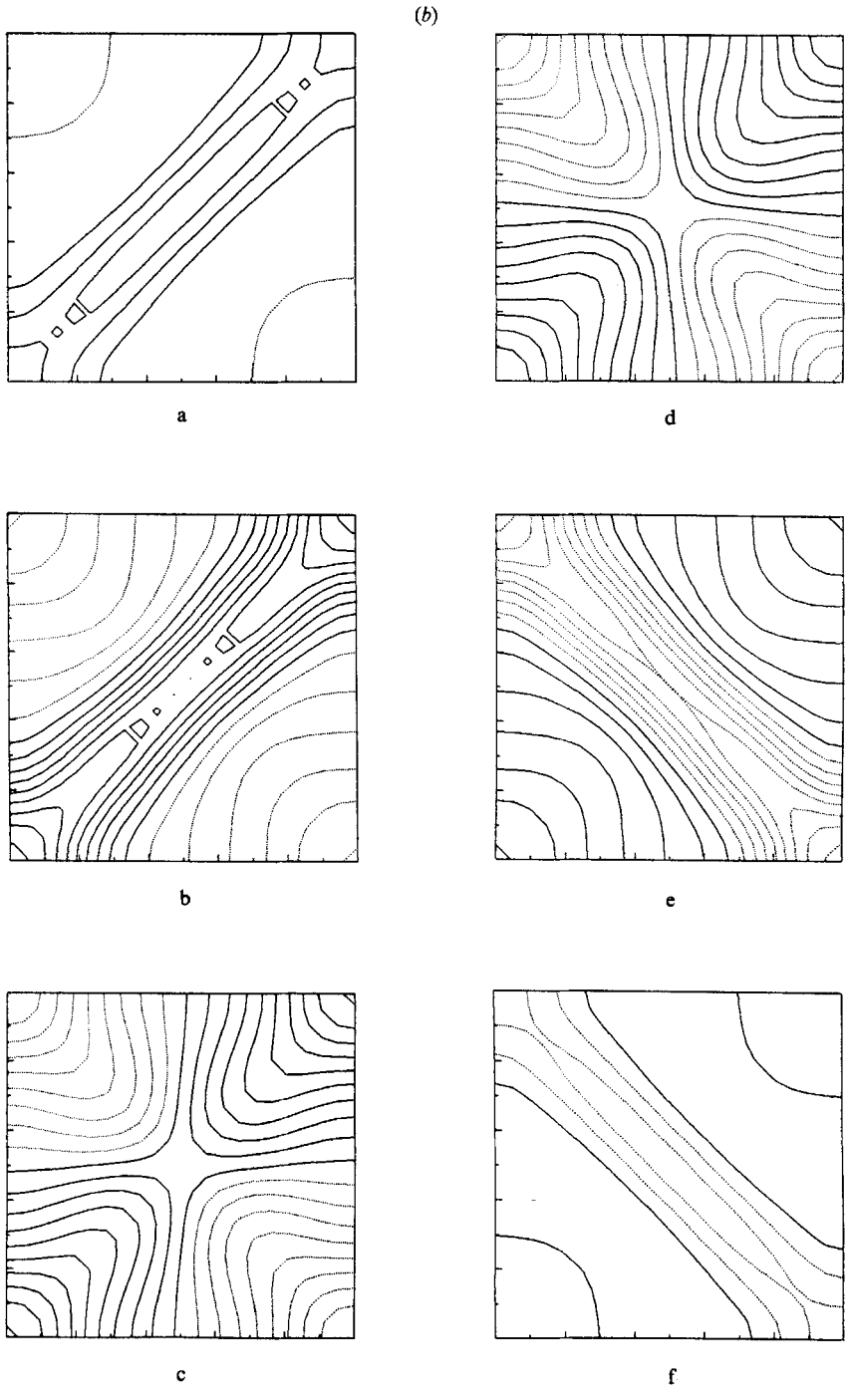

FIGURE 3(*b*). For caption see facing page.

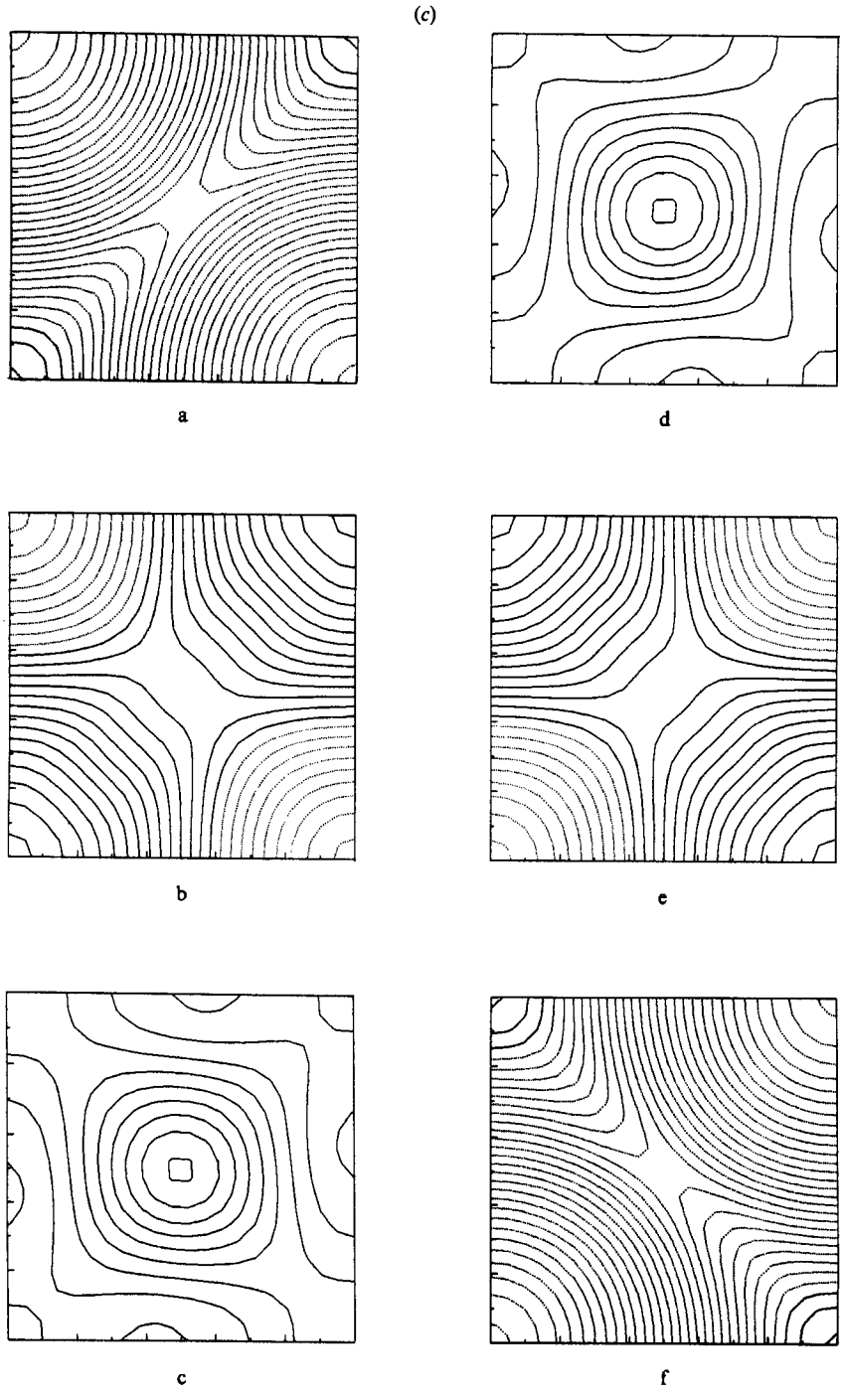

FIGURE 3. (*a*) Isotherms of θ, (*b*) the contours of w, and (*c*) the contours of ϕ_ζ at each horizontal cut at $R = 250$ ($N = 20$). θ is the measure of deviation from the conduction profile. The interval of the isotherms is 0.05. Hot isotherms are shown solid and cold ones are dotted. The contour interval of w is 8. Upward flows are shown solid and downward ones are dotted. The contour intervals of ϕ_ζ are 0.5 for b–e and 1 for a and f. The flows are perpendicular to the contour lines. Solid lines show positive values and dotted lines show negative values.

Location	$N = 20$	$N = 26$	$N = 30$	$N = 34$
a	0.043	0.037	0.032	0.029
b	0.238	0.260	0.290	0.230
c	0.476	0.480	0.484	0.486
d	0.524	0.520	0.516	0.514
e	0.762	0.740	0.710	0.770
f	0.952	0.963	0.968	0.971

TABLE 1. Vertical position of horizontal cross-sections (a–f) for various truncation numbers

section; the rest of it is filled with the descending cold fluid. As the hot material ascends beyond $\zeta = 0.5$, the hot area continues to expand and fills most of the cross-section, except for the pair of diagonally opposing corners where cold descending fluid is found. Figure 3(*b*) shows the vertical velocities in the same horizontal planes. A strong correlation between figures 3(*a*) and 3(*b*) is apparent: hot and cold zones correspond to upward and downward flows, respectively. Figure 3(*c*) shows the horizontal velocity potential ϕ_ζ; the horizontal velocities are perpendicular to the contours. Figure 4(*a–c*) shows isotherms and flow patterns at $R = 450$. Though this flow is similar to the one at $R = 250$, convection at the higher Rayleigh number is much more vigorous. For example, in figure 4(*a*, *b*), the diagonal upward flow is distinctive and much stronger than the downward flow. The symmetries about the two diagonals in each horizontal plane and the antisymmetries with respect to the reflection plane at $\zeta = 0.5$ characterize the flow fields in figures 3 and 4. The spectral coefficients that would make non-symmetric contributions to these flow fluids remain on the order of the round-off error and show no tendency to grow during the computations.

3.2. *Steady-state convection with partial symmetry breaking*: S′

As the Rayleigh number is increased from $R = 500$ to $R = 550$ the solutions begin to lose the symmetry about the two diagonals in each horizontal plane. Figure 5(*a–c*) shows the loss of this symmetry in both temperature and flow fields at $R = 550$. In these steady-state flows, the rising and sinking motion near the lower and upper walls shifts slightly to off-diagonal positions. However, the convection pattern at $R = 550$ still exhibits antisymmetry with respect to $\zeta = 0$ and a 90° rotation about the axis $\xi = \eta = 0.5$. (The corresponding conditions on the indices of the spectral coefficients are that either $n+m$ or $n+j$ is even.) We confirmed the partial symmetry breaking with truncation numbers $N = 26$ and 30 and refer to this solution as S′. The S′ solution closely resembles Horne's (1979) finite-difference solution at $R = 300$. Partial symmetry breaking at $R = 300$ in Horne's solution may be due to the relatively coarse grid ($17 \times 17 \times 17$) he employed.

To further characterize the existence of S and S′, we show the ratio of Φ_{101} to Φ_{111} as a function of R in figure 6. (Φ_{101} is a fundamental spectral coefficient of flows which are not symmetric about diagonals in horizontal planes.) The figure shows the coexistence of the two branches in the range between $R = 475$ and $R = 540$ as a consequence of hysteresis. With increasing R, the S→S′ transition takes place between $R = 540$ and 545. With decreasing R, the S′ state persists for R as low as 475. The value of R at which S changes to S′, or vice versa, depends on the rate at which R is increased or decreased. When R was increased in one step from 500 to 540, we found that Φ_{101}/Φ_{111} was about 0.3 at $R = 540$, already large enough to characterize

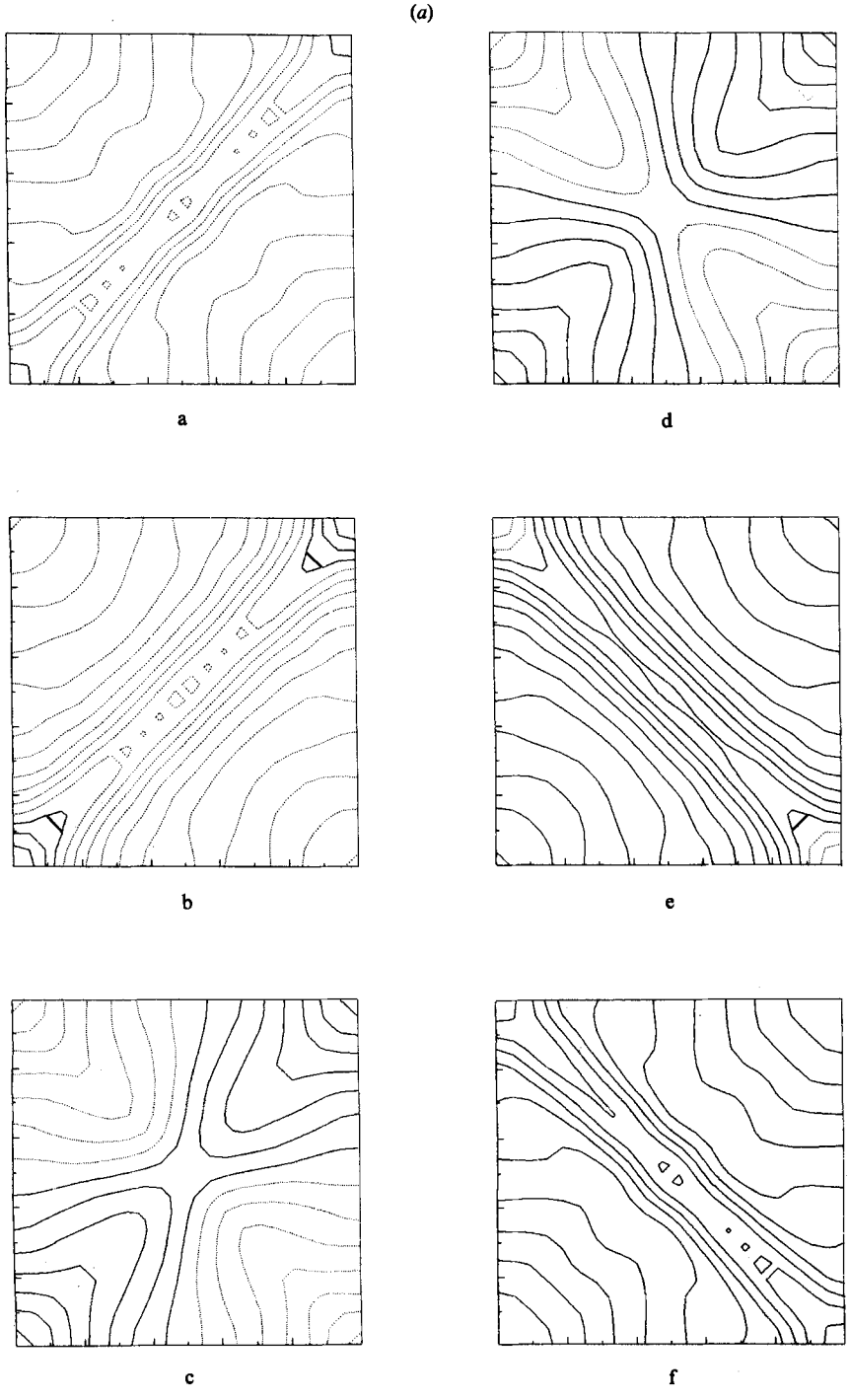

FIGURE 4(*a*). For caption see page 165.

(*b*)

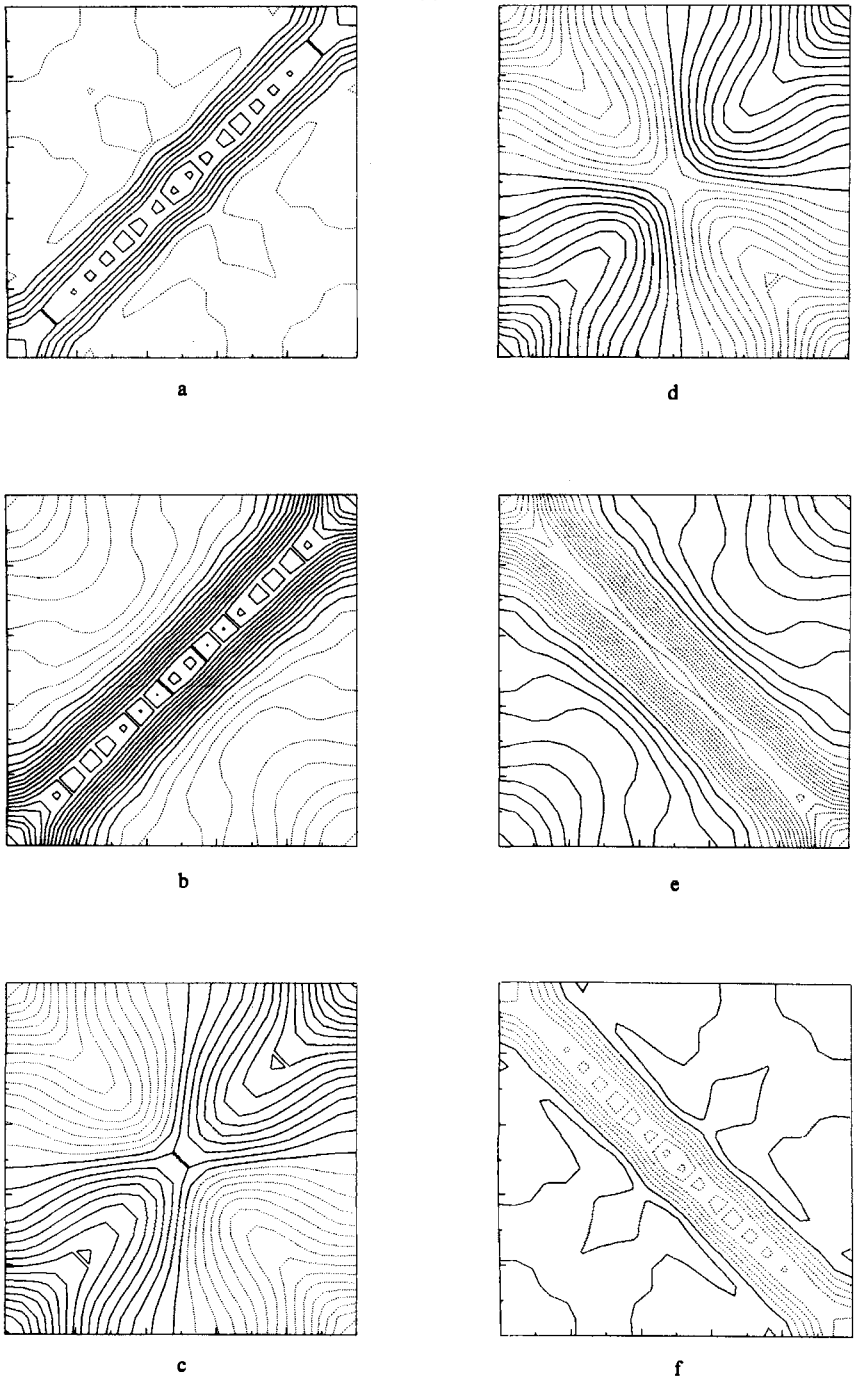

FIGURE 4(*b*). For caption see facing page.

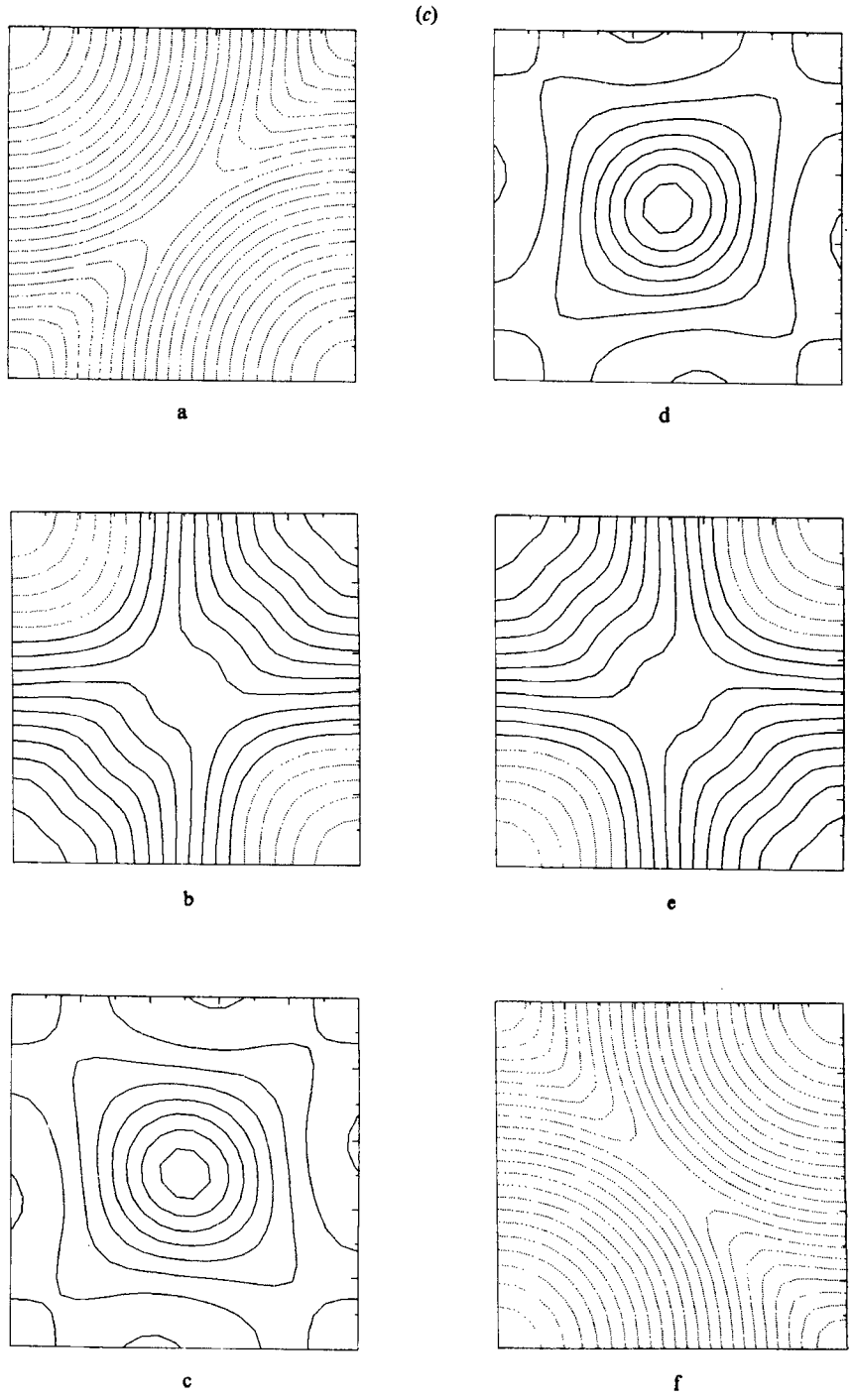

FIGURE 4. (*a*) isotherms of θ, (*b*) contours of w, and (*c*) contours of ϕ_ζ at each horizontal cut when $R = 450$ and $N = 20$. The intervals of θ and w are 0.05 and 8 respectively. The contours of ϕ_ζ are 1 for b–e and 2 for a and f.

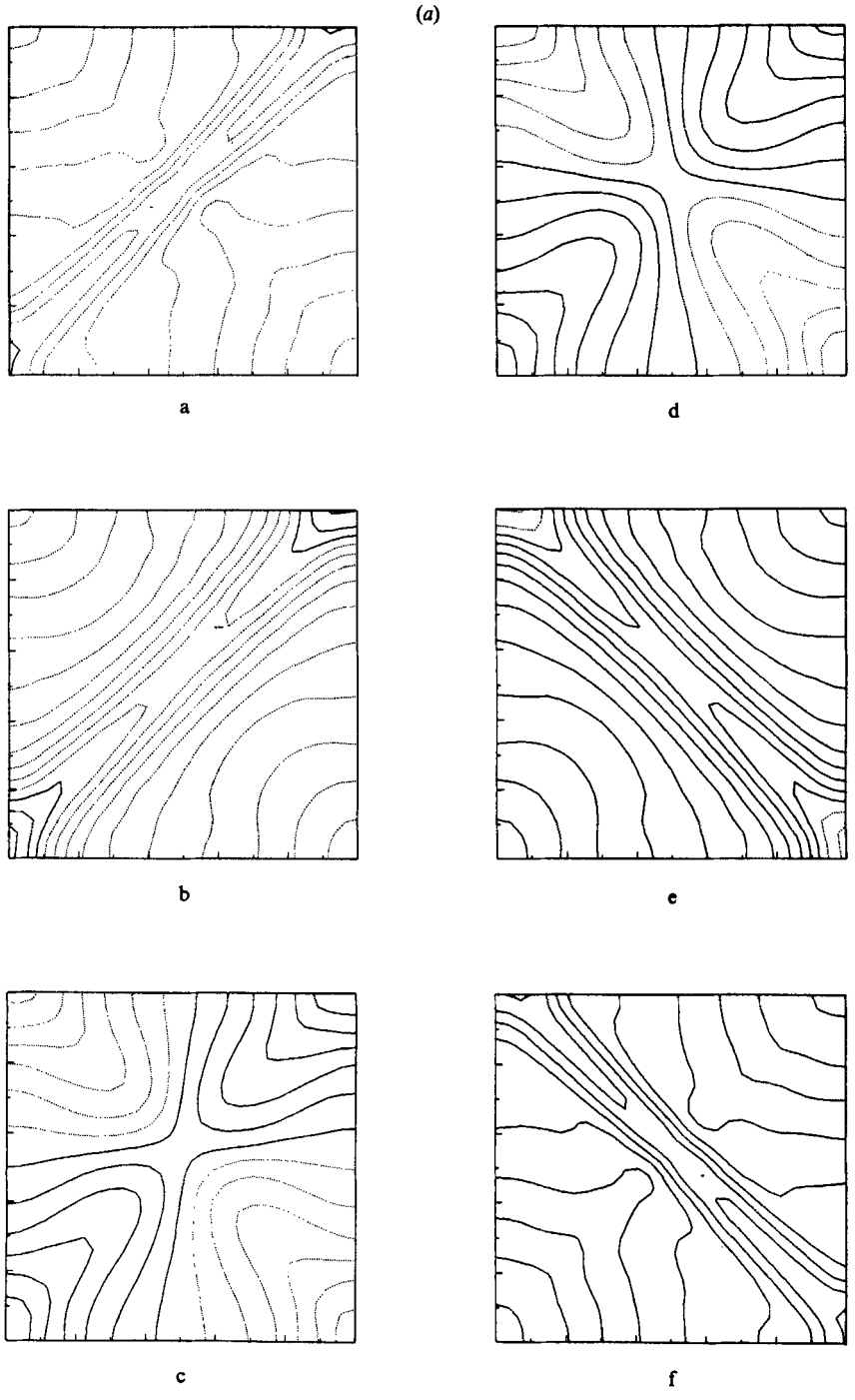

FIGURE 5(a). For caption see page 168.

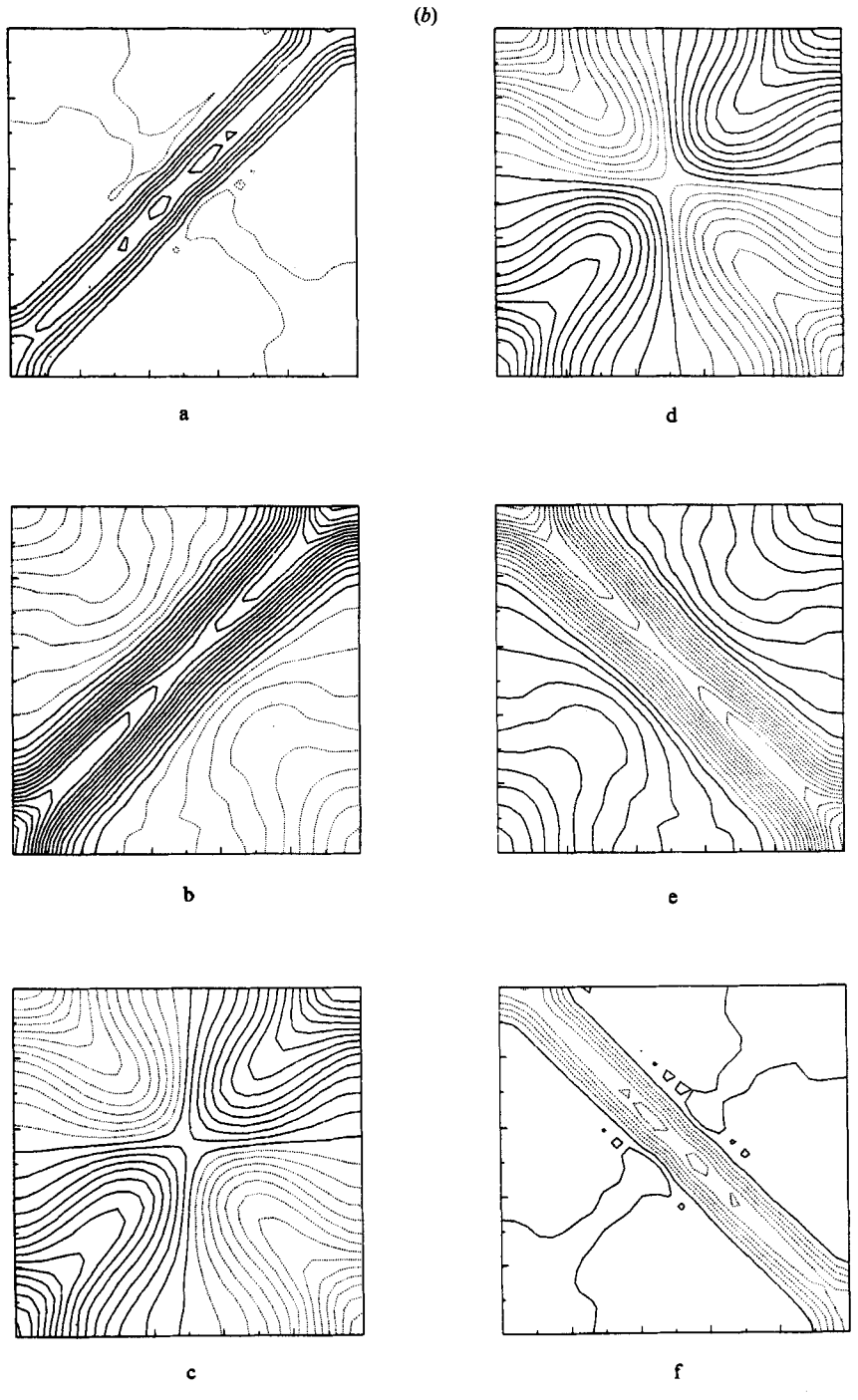

FIGURE 5(*b*). For caption see page 168.

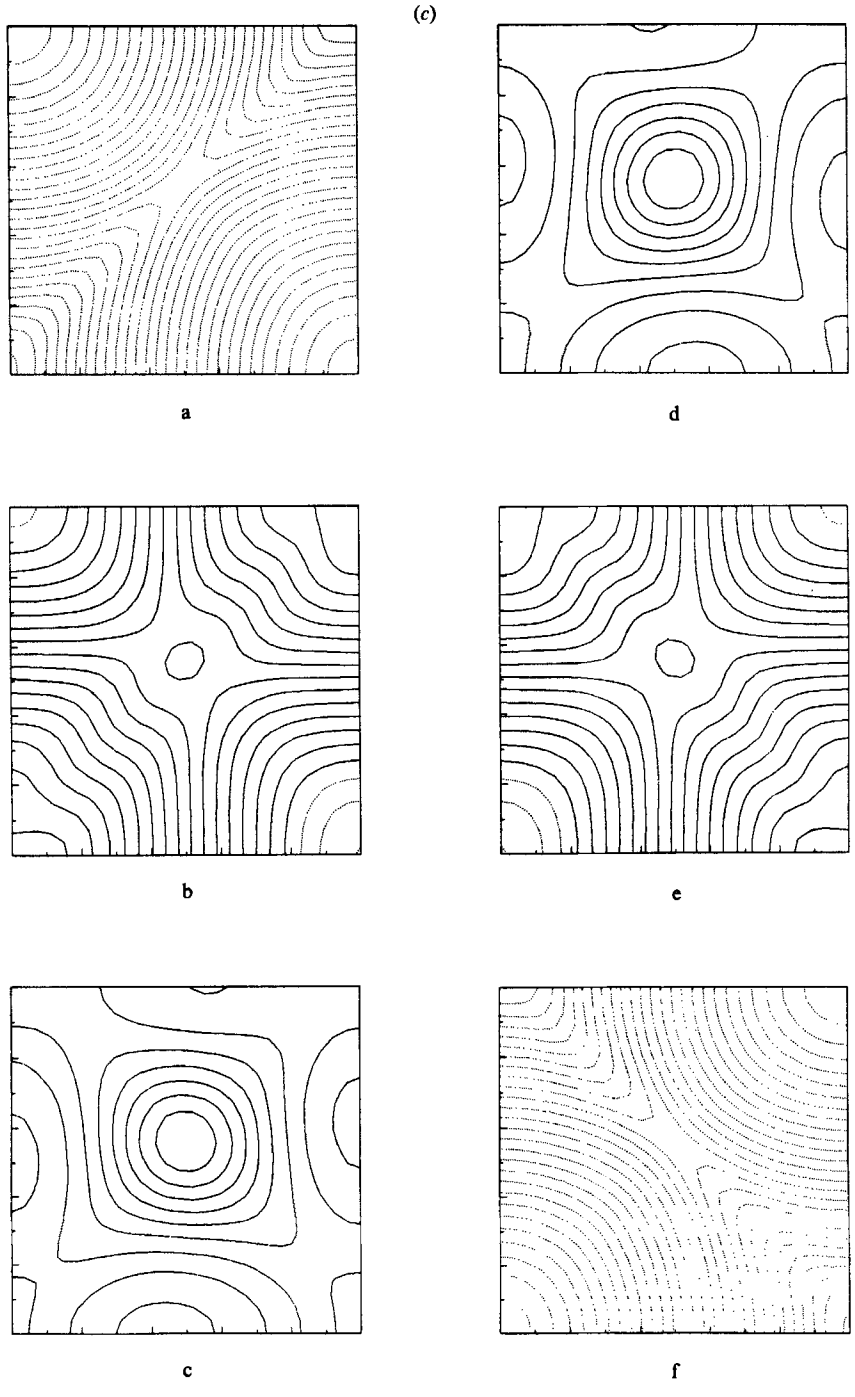

FIGURE 5. (*a*) isotherms of θ, (*b*) contours of w, and (*c*) contours of ϕ_ζ at each horizontal cut at $R = 550$ ($N = 26$). The contour intervals of θ and w are 0.05 and 10. The contour intervals of ϕ_ζ are 1 for b–e and 2 for a and f.

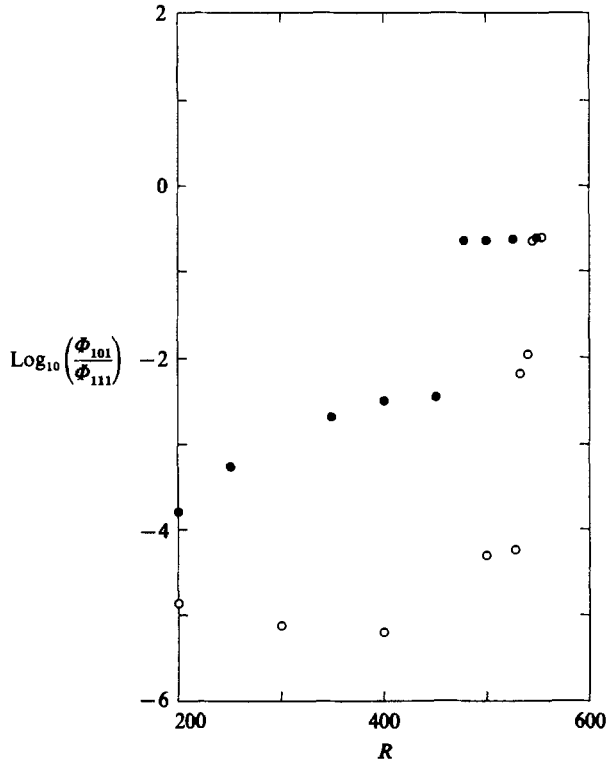

FIGURE 6. $\mathrm{Log}_{10}(\Phi_{101}/\Phi_{111})$ as a function of increasing R(○) or decreasing R(●).

the flow as S′. However, upon increasing R in two steps (500 → 530 → 540), the flow at $R = 540$ effectively retained the symmetries about the horizontal diagonals; the ratio Φ_{101}/Φ_{111} was about 0.01. By decreasing the Rayleigh-number step size it is probable that we would increase the value of R for the S → S′ transition (or vice versa for S′ → S). As indicated by the gradual growth of the ratio Φ_{101}/Φ_{111} when R is greater than 530, however, it appears that the transition S → S′ is inevitable. The S′ state transfers slightly less heat than does the S-state; for example, a 0.3% difference in heat transfer is observed at $R = 500$. The dependence of the S → S′ transition on the Rayleigh number step size raises the possibility that this transition might not occur before S → $\mathrm{P}^{(1)}$ for sufficiently small steps in R.

3.3. *Simply periodic state*: $\mathrm{P}^{(1)}$

At $R = 575$ the solution is oscillatory. The temporal behaviour of the Nusselt number during the early part of the computations is shown in figure 7. After large overshoots and undershoots, $Nu(\tau)$ first appears to approach a steady state, but it soon starts to oscillate with small but steadily growing amplitude. It is found that the system evolves to a simply periodic state $\mathrm{P}^{(1)}$ after a sufficiently long time integration, typically 0.7–1.0 in non-dimensional time. We confirmed the transition from S′ to $\mathrm{P}^{(1)}$ with $N = 26$ and 30. Our best estimate for the transition Rayleigh number is somewhere between 550 and 575. Figure 8 shows a representative Nusselt-number oscillation with time about the mean value at $R = 625$. The spectral power plot has peaks only at a single frequency f_1 and its harmonics.

Since the characteristics of time-dependent states are sensitive to aliasing and the

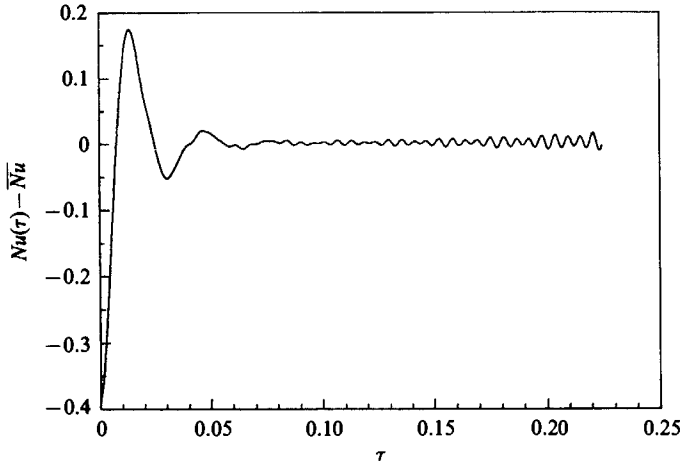

FIGURE 7. Onset of simply periodic oscillatory convection at $R = 575$ ($N = 26$). This time integration was initiated using the final solution at $R = 550$ as the initial condition.

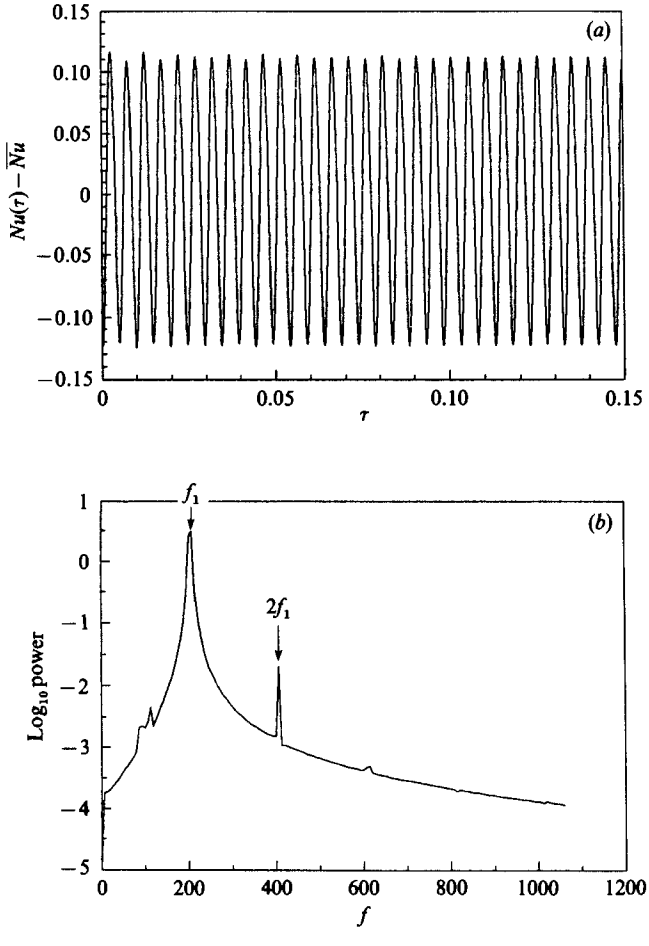

FIGURE 8. (*a*) The time series $Nu(\tau)-\overline{Nu}$ and (*b*) its power spectrum in a simply periodic flow at $R = 625$ ($N = 26$).

Number of added zeros	Average Nusselt number, $\overline{Nu}$	Oscillation frequency of $Nu(\tau)-\overline{Nu}$	Frequency resolution	Variance of $Nu(\tau)-\overline{Nu}$
2	7.48688	176.6	3.9	1.359×10^{-4}
7	7.48747	176.6	3.9	1.349×10^{-4}
11	7.48747	176.6	3.9	1.349×10^{-4}

TABLE 2. Test on aliasing effects. $R = 580$, $N = 26$ with diagonal truncation $\Delta\tau = 0.7494\times10^{-4}$, number of time steps = 3400. The number of added zeros is varied.

Time step	Average Nusselt number, $\overline{Nu}$	Frequency of largest spectral peak of $Nu(\tau)-\overline{Nu}$	Frequency resolution	Variance of $Nu(\tau)-\overline{Nu}$
0.7494×10^{-5}	7.48747	176.6	3.9	1.349×10^{-4}
0.3747×10^{-4}	7.48679	172.7	3.9	1.322×10^{-4}

TABLE 3. Tests on the accuracy of the time integration. The conditions are the same as those with seven added zeros in table 2, except the time step, which is halved in the second case.

integration time step, we have carried out a number of tests on the accuracy of our numerical results. First, we varied the number of added zero-value coefficients and performed three computations with other parameters fixed ($R = 580$, $N = 26$, $\Delta\tau = 7.494\times10^{-5}$). Table 2 shows the resulting time-averaged Nusselt number Nu, oscillation frequency and Nu variance. All of these quantities agree to at least three significant figures. The effectiveness of adding only a small number of zero-valued coefficients in reducing aliasing is probably due to the use of diagonal truncation. In the present study, we have always added 5 to 7 zeros in order to ensure effectively alias-free results.

Next we performed the same calculation ($R = 580$, $N = 26$ and seven zeros added) using two different time steps. A second-order Runge–Kutta technique was used in the time integration of the spectral coefficients. Results for two different time steps are shown in Table 3. The time-averaged Nusselt numbers agree to three significant figures. The variance and the oscillation frequency of $Nu(\tau)$ differ by 2%. The frequency peak shifts to the nearest lower value when the time-step is halved. However, in these cases, both $f = 176.6$ and $f = 172.7$ are strong spectral peaks of almost equal magnitude. The true frequency probably lies somewhere between the two. This comparison indicates that the time integration is accurate enough in determining both time-averaged and oscillatory characteristics.

The sampling interval for analysing the oscillatory characteristics of $Nu(\tau)$ is equal to the time step used in the time integration. Since the time integration is performed explicitly, the time step is restricted by the Courant number, which decreases with increasing truncation number. Sampling intervals used in the spectral analysis for three different truncation numbers are shown in table 4. The frequency resolution, or the lowest frequency contained in the spectral analysis, on the other hand, is determined by the length of the time integration. Normally the lengths of the integrations were 0.2–0.3 in non-dimensional time. Therefore, typical frequency resolutions are from 3–5, corresponding to 1–2% of the frequency peak in a simply periodic state. Frequency resolutions for several cases are shown in table 5.

Representative contours for θ, w and ϕ_ζ in each horizontal plane are shown in

Truncation number, N	Sampling interval
26	0.7494×10^{-4}
30	0.5629×10^{-4}
34	0.4384×10^{-4}

TABLE 4. Sampling intervals for analysing the spectral content of $Nu(\tau) - \overline{Nu}$. These are equal to the time steps used in computations with the indicated truncation numbers.

Figure number	Rayleigh number	Frequencies of largest spectral peaks	Frequency resolution
8	640	f_1 204.4	4.4
13(*a*)	680	f_3 97.7 f_2 142.1 f_1 284.2	8.9
13(*b*)	680	f_3 96.4 f_2 126.9 f_1 248.7	5.1
14	740	f_3 136.9 f_2 165.4 f_1 302.3	5.7

TABLE 5. Frequency resolutions of representative computations

figure 9(*a–c*). The contours of these quantities in the planes at b, c, d and e show almost identical features to those in the S′ state. Within the top and bottom boundary layers, however, ripple-like disturbances in the θ- and w-fields are evident; these indicate that boundary-layer instability may be the cause of the oscillation in the Nusselt number. Despite the ripple-like patterns within the θ boundary layer, horizontal flows are surprisingly smooth and do not show any irregularity. Figure 10(*a, b*) shows the contours of w in the horizontal planes a and f at six equally spaced times within a single oscillation period. The ripple-like disturbances gradually move towards the band-like ascending or descending flows near diagonals, and they are eventually engulfed by the main flows; ripples are generated repeatedly. The maximum of the vertical velocity in the top and bottom boundary layers varies by approximately 15% of the average value during the period; vertical velocity assumes its maximum value shortly after the ripples are engulfed. Antisymmetry about $\zeta = 0.5$ with a 90° rotation about $\xi = \eta = 0.5$ can be seen by comparing equally numbered plates in figures 10(*a*) and 10(*b*).

The system remains in the $P^{(1)}$ state until another time-dependent state replaces it at a higher Rayleigh number. The characteristics of the $P^{(1)}$ state are summarized in figures 11 and 12. Figure 11 shows the fundamental oscillation frequency as a function of R. The non-dimensional frequency at onset of time dependence ($R = 575$) is 175 ± 3. The frequency increases with R according to $f \propto R^{2.1}$. The variance also increases by an order of magnitude as R increases from 580 to 640. At $R = 640$, near the end of the $P^{(1)}$ Rayleigh number interval, the frequency exhibits an abrupt increase to $f = 250$, which is higher by 40 than the value predicted by extension of the trend from lower values of R. The frequency of 250 at $R = 640$ has been confirmed with three different truncation numbers, $N = 26$, 30 and 34. Kimura *et al.* (1987) showed the presence of a quasi-periodic state in a narrow range between $R = 625$ and $R = 640$.

(*a*)

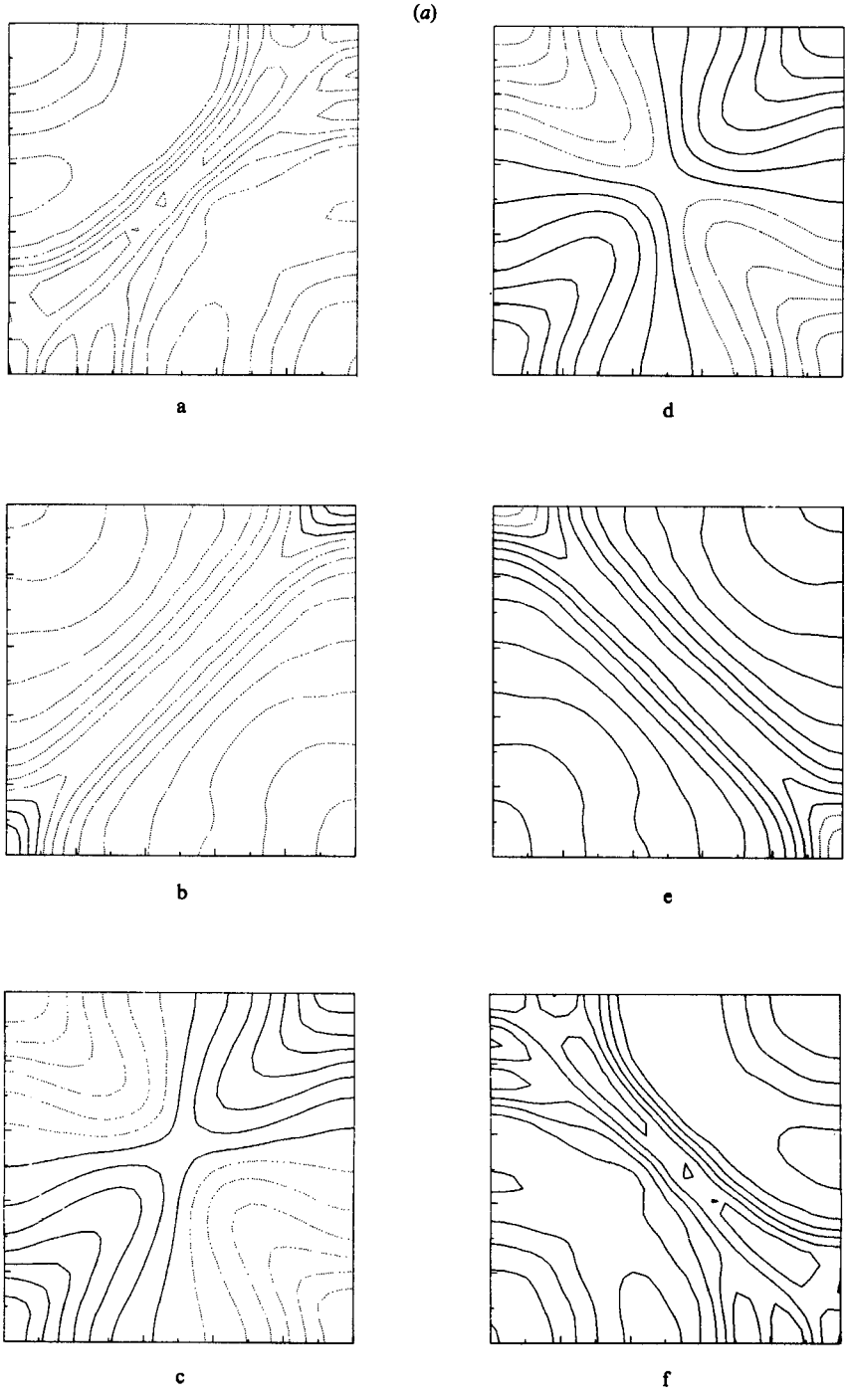

FIGURE 9(*a*). For caption see page 175.

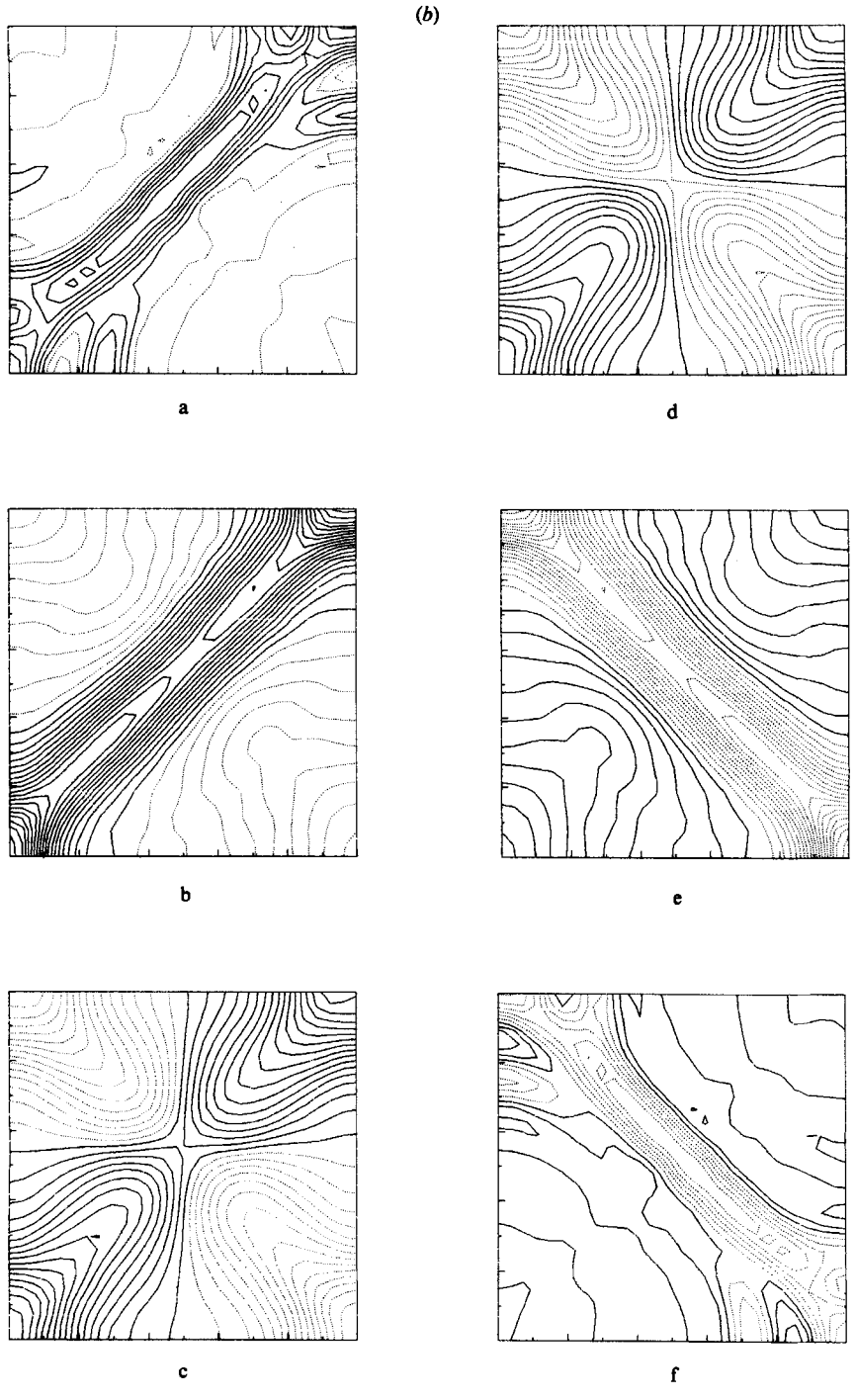

FIGURE 9(b). For caption see facing page.

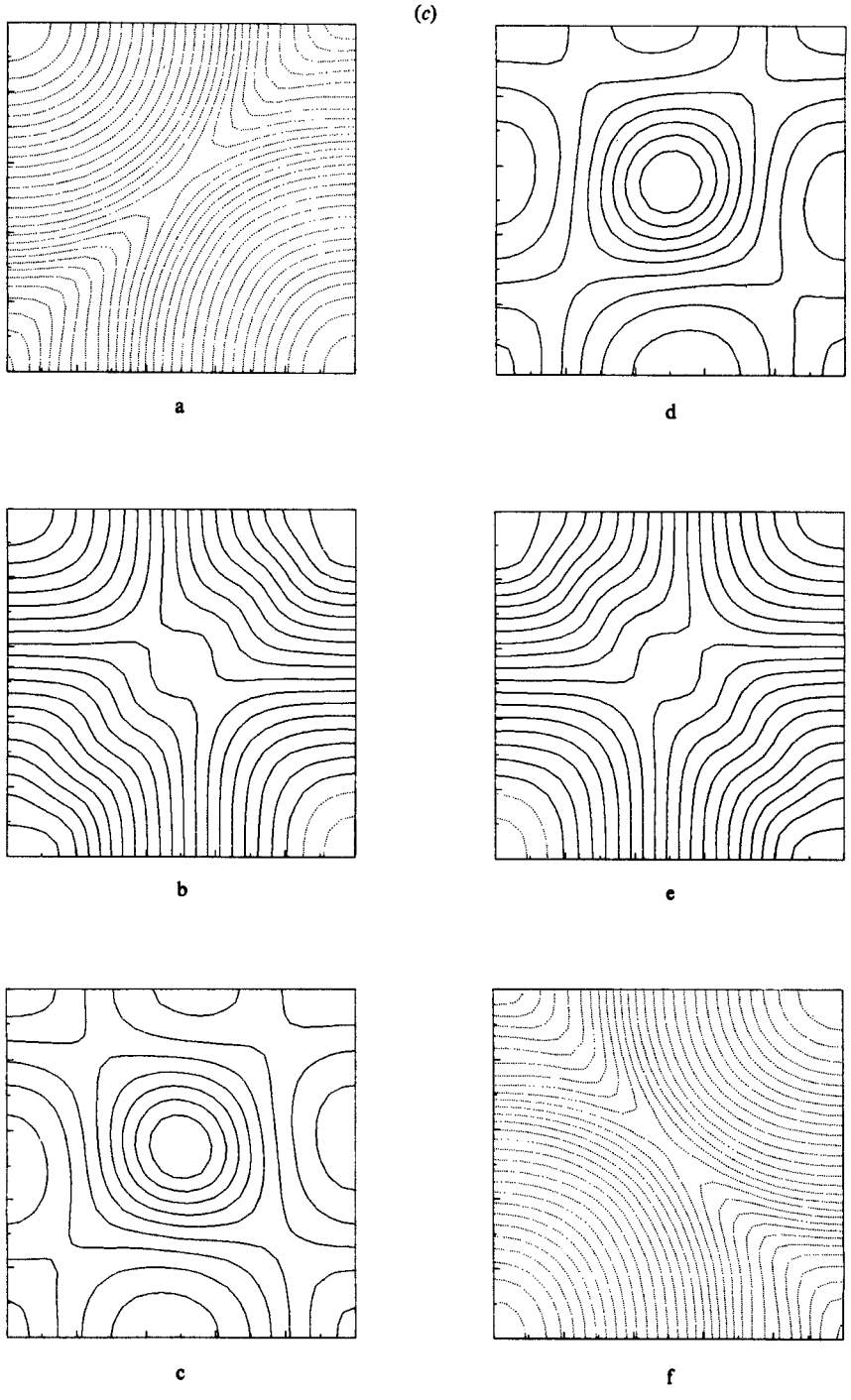

FIGURE 9. (*a*) isotherms of θ, (*b*) the contours of w, and (*c*) the contours of ϕ_ζ at each horizontal cut during a simply periodic oscillatory convection at $R = 625$ ($N = 26$). The contour intervals of θ, w and ϕ_ζ are the same as those in figure 5.

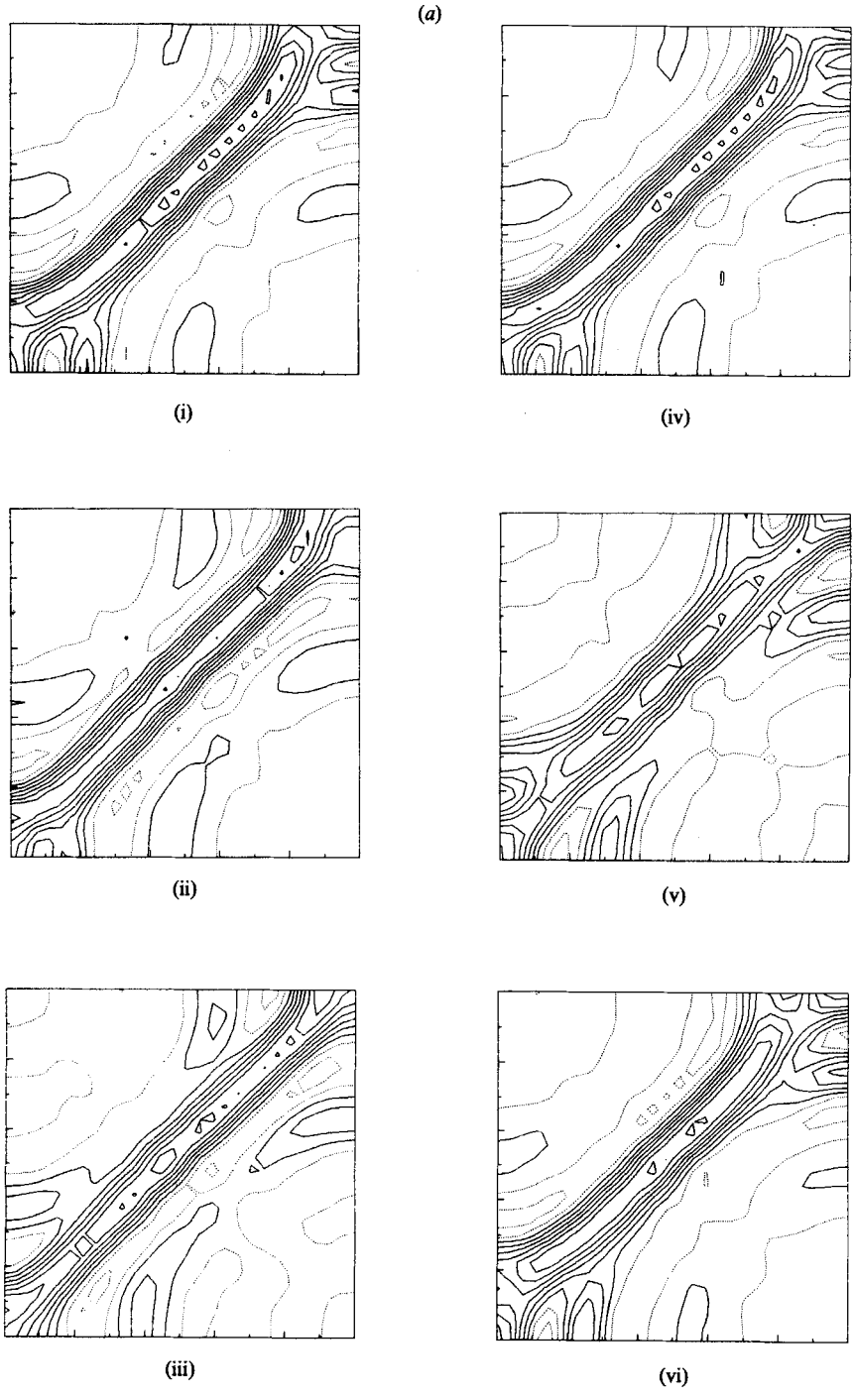

FIGURE 10(*a*). For caption see facing page.

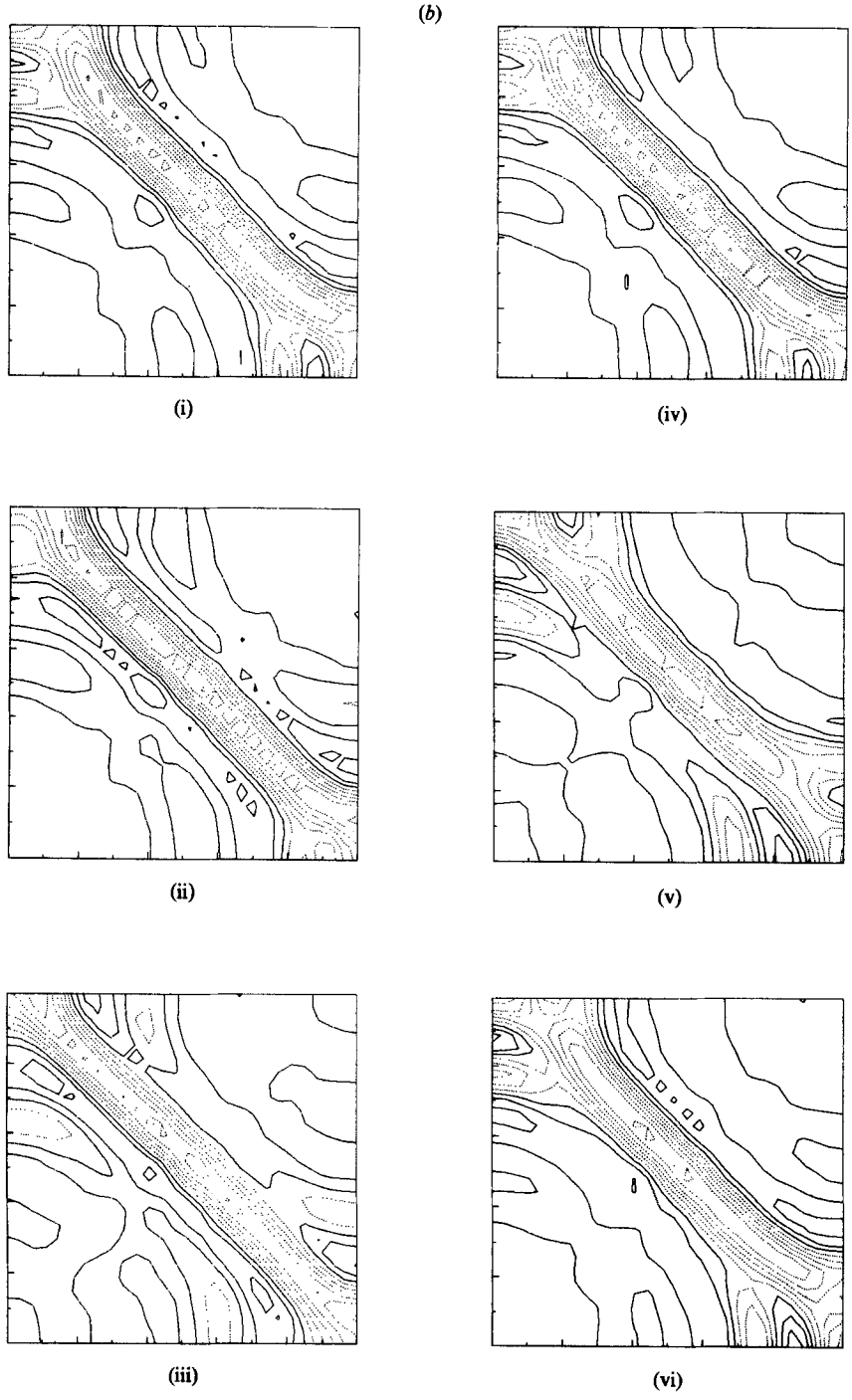

FIGURE 10. Contours of w in horizontal cuts at vertical positions a and f when $R = 625$ and $N = 26$. The contour interval is 10. Plates (i)–(vi) show flows at six consecutive times during a single period, where $\Delta\tau = 8.24 \times 10^{-4}$. (*a*) the horizontal cut at the vertical position f. Anti-*symmetry with* respect to $\zeta = 0.5$ and a 90° rotation about $\xi = \eta = 0.5$ are seen at equally numbered plates. (*b*) The horizontal cut at the vertical position a.

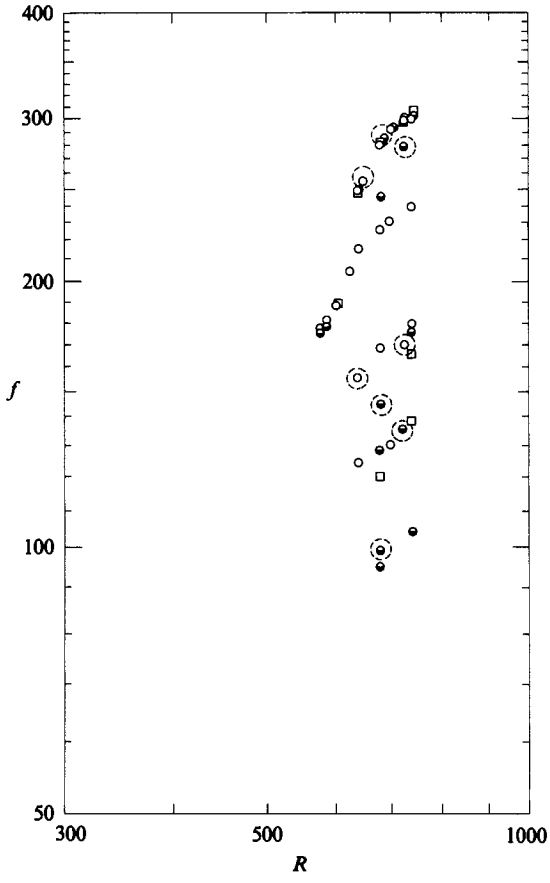

FIGURE 11. Dimensionless frequencies f of the peaks in the spectral power of $Nu(\tau)-\overline{Nu}$ as function of R. ○, $N=26$; ◒, $N=30$; □, $N=34$. Dotted circles indicate the peaks observed in a different oscillatory regime at the same Rayleigh number.

3.4. *Quasi-periodic state*: QP_2 *or* QP_3

When the Rayleigh number is increased further above $R=650$ with $N=26$ or $N=30$, the system evolves to a somewhat complex time-dependent state characterized by two or three incommensurate frequencies. We have found characterization of the quasi-periodic state in a cube to be a much more difficult task than its two-dimensional counterpart. We accumulated the $Nu(\tau)$ data up to $\tau=0.7$–1.0 in non-dimensional time before determining properties of the time-dependent convection. However $Nu(\tau)$ is not always characterized by a unique oscillatory state for a given Rayleigh number (at a fixed truncation number) as described in our earlier work on two-dimensional flows (Schubert & Straus 1982; Kimura *et al.* 1986). A quasi-periodic state sometimes consists of two or more distinctive states, each of which lasts for $\tau=0.2$–0.3, has spectral peaks at different frequencies, and has different values of variance and average Nusselt number. An example for $R=680$ and $N=30$ is shown in figure 13(*a*,*b*). Figure 13(*a*) shows $Nu(\tau)$ and its spectrum during an early stage; $\tau=0$ corresponds to approximately 0.2 non-dimensional time units after time integration was initiated. Spectral peaks occur at $f_3=98\pm5$, $f_2=142\pm5$ and $f_1=284\pm5$. The variance is about 0.0074. These are indicated by dashed circles in figures 11 and 12. Further time integration transforms $Nu(\tau)$ to that in figure 13(*b*), where

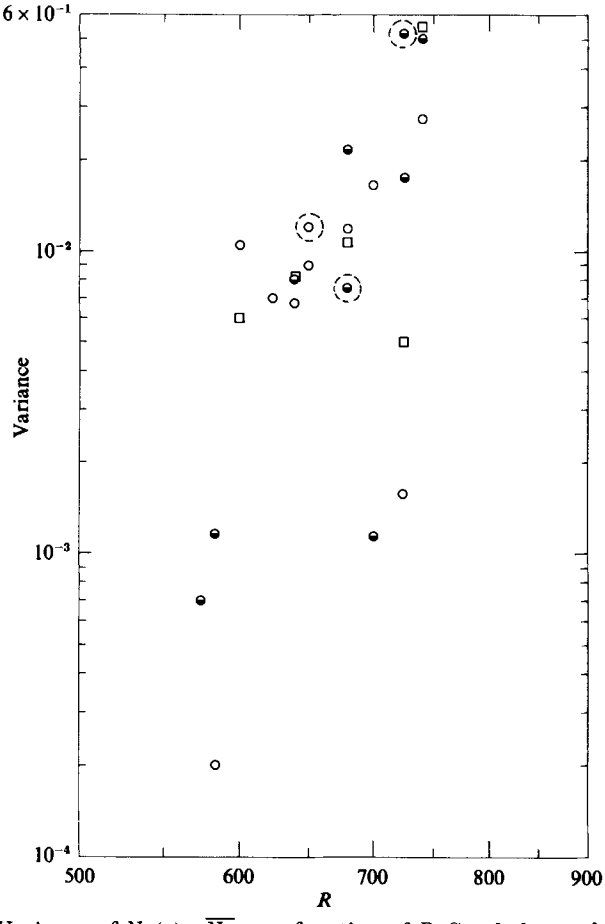

FIGURE 12. Variance of $Nu(\tau)-\overline{Nu}$ as a function of R. Symbols are defined in figure 11.

the amplitude of oscillation is greater and its basic frequencies are $f_3 = 96\pm3$, $f_2 = 127\pm3$ and $f_1 = 249\pm3$.

It has been observed that the transition described above often occurs when the time-integration is interrupted and continued at the same values of R and N. The continuing-integration process involves a switch of time-integration scheme from the second order Runge–Kutta to the first-order Euler scheme at the very first time-integration step. It is conceivable that the transition may be caused by errors introduced during the restarting process, although there has not been any evidence of this in two-dimensional calculations. Quasi-periodic three-dimensional convection may therefore be very sensitive to introduced disturbances. We observed similar transitions at $R = 650$ with $N = 26$ and $R = 725$ with $N = 30$. The spectral characteristics and the variances corresponding to different regimes are marked with dashed circles in figures 11 and 12. Although variances change from one regime to another without identifiable trends, the spectral contents vary in a somewhat consistent way. High-frequency peaks are found on the simply periodic trend $f \propto R^{2.1}$ extended beyond $R = 640$. The high-frequency peaks occur near $f = 100$, 130 and 170. The frequencies of each of these peaks increase with R.

With $N = 26$ and 30, the quasi-periodic states revert with increasing R to another simply periodic state with a drastic reduction in variance. A similar decrease in

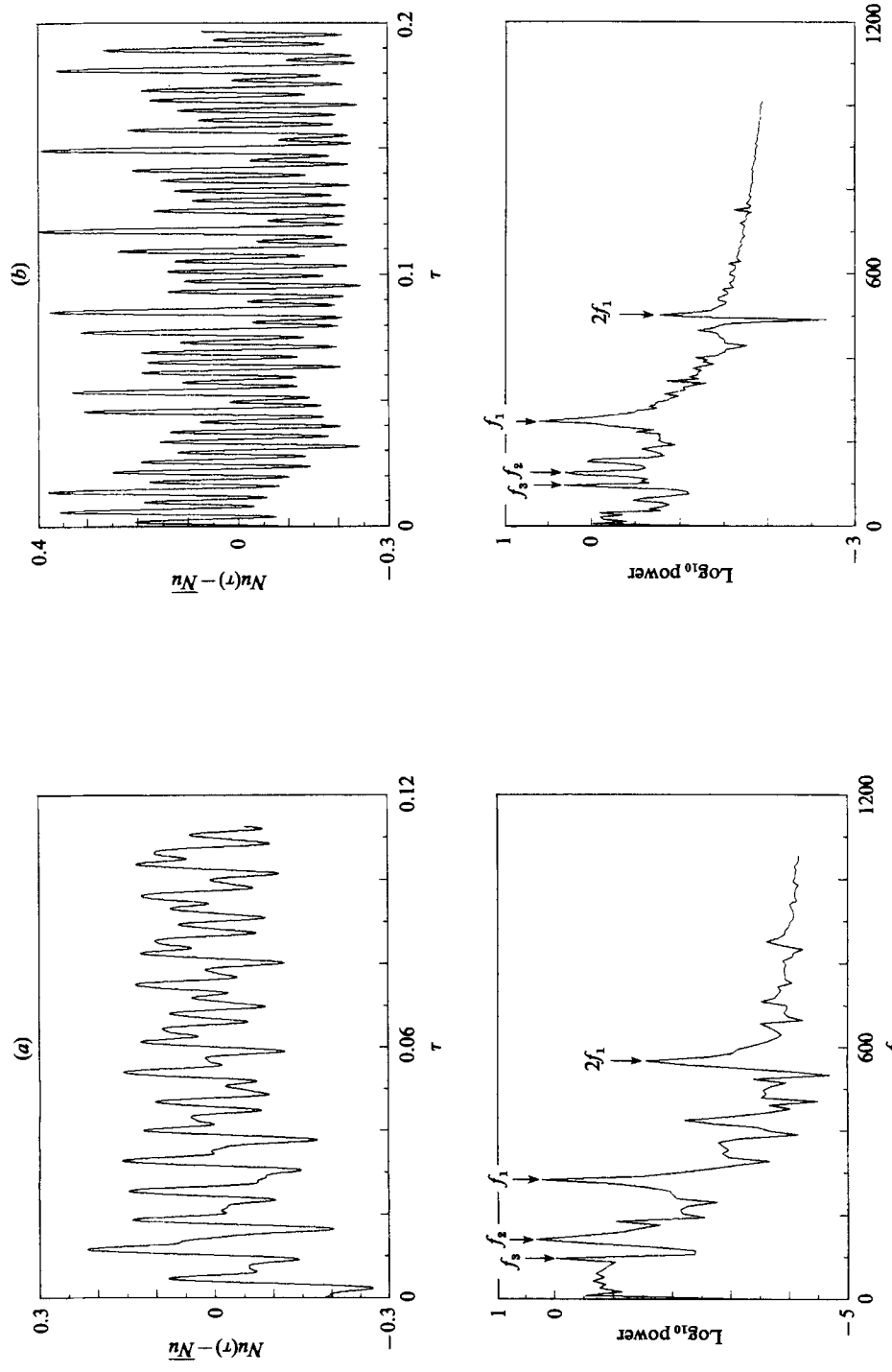

FIGURE 13. The time series $Nu(\tau)-\overline{Nu}$ and its power spectrum at $R = 680$ ($N = 30$). $\tau = 0$ in the $(Nu(\tau)-\overline{Nu})$–τ diagram corresponds to approximately (*a*) 0.2 and (*b*) 0.5 in non-dimensional time after the time integration at $R = 680$ was initiated.

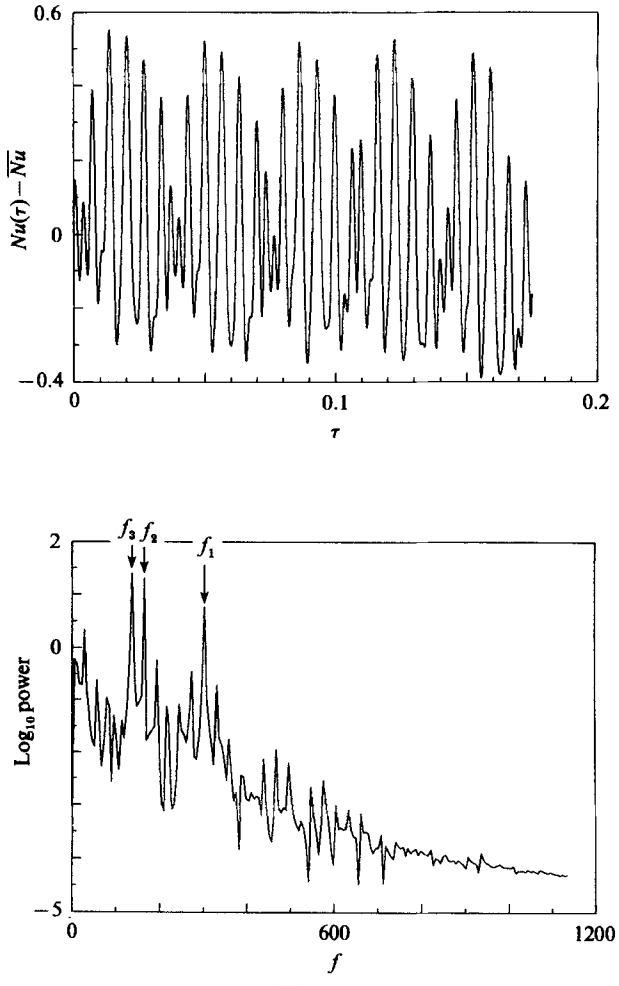

FIGURE 14. The time series of $Nu(\tau)-\overline{Nu}$ and its power spectrum at $R = 740$ ($N = 34$).

variance has been observed when the system develops from a quasi-periodic state to a simply periodic state in two-dimensional flows (Schubert & Straus 1982). We confirmed this transition with a higher truncation number $N = 34$.

The increase of R from 725 to 740 transforms the system again to a quasi-periodic state. Figure 14 shows $Nu(\tau)$ and its spectral content at $R = 740$. Temperature and flow fields are shown in figure 15 (a–c). Several new features are seen in these figures. Disturbances originating from the thermal boundary layers penetrate more deeply into the core flow than was the case at $R = 625$. They are identified by hot rising or cold descending spots in the horizontal midplanes (plates b–e). The horizontal flows within the top and bottom boundary layers are no longer smooth, as evidenced by distorted isopotential lines ϕ_ξ (in plates a and b in figure 15). Figure 16 shows a series of contour diagrams of w at successive times. Comparison with figure 10 (a, b) shows that disturbances within the boundary layers are of smaller scales, probably due to thinner thermal boundary layers. Despite this complex vertical-flow structure within the thermal boundary layers, the antisymmetry about $\zeta = 0.5$ and a 90° rotation about $\xi = \eta = 0.5$ are still present at $R = 740$ (see plates a and f in figure 16b), the highest Rayleigh number in the present study.

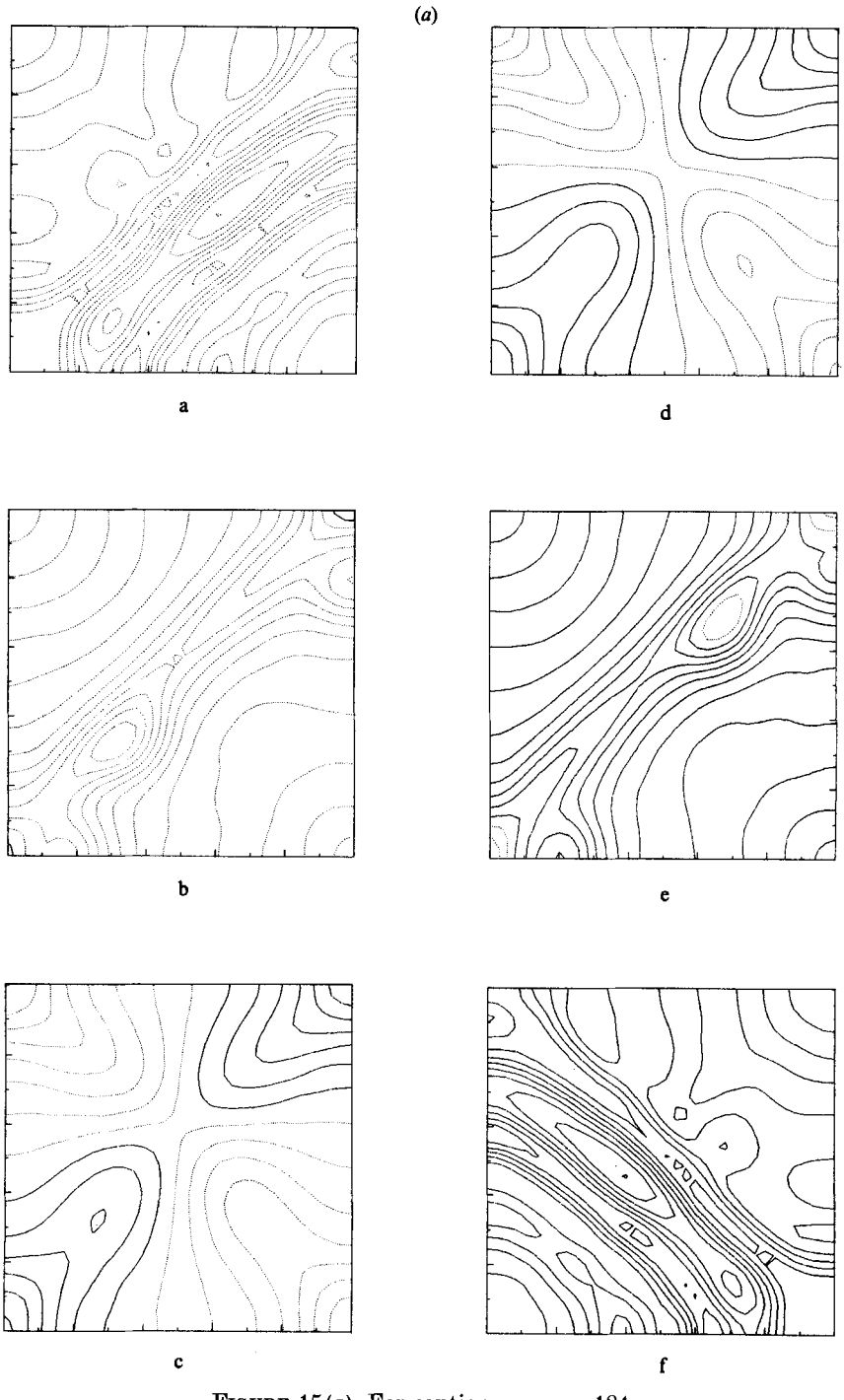

FIGURE 15(a). For caption see page 184.

(*b*)

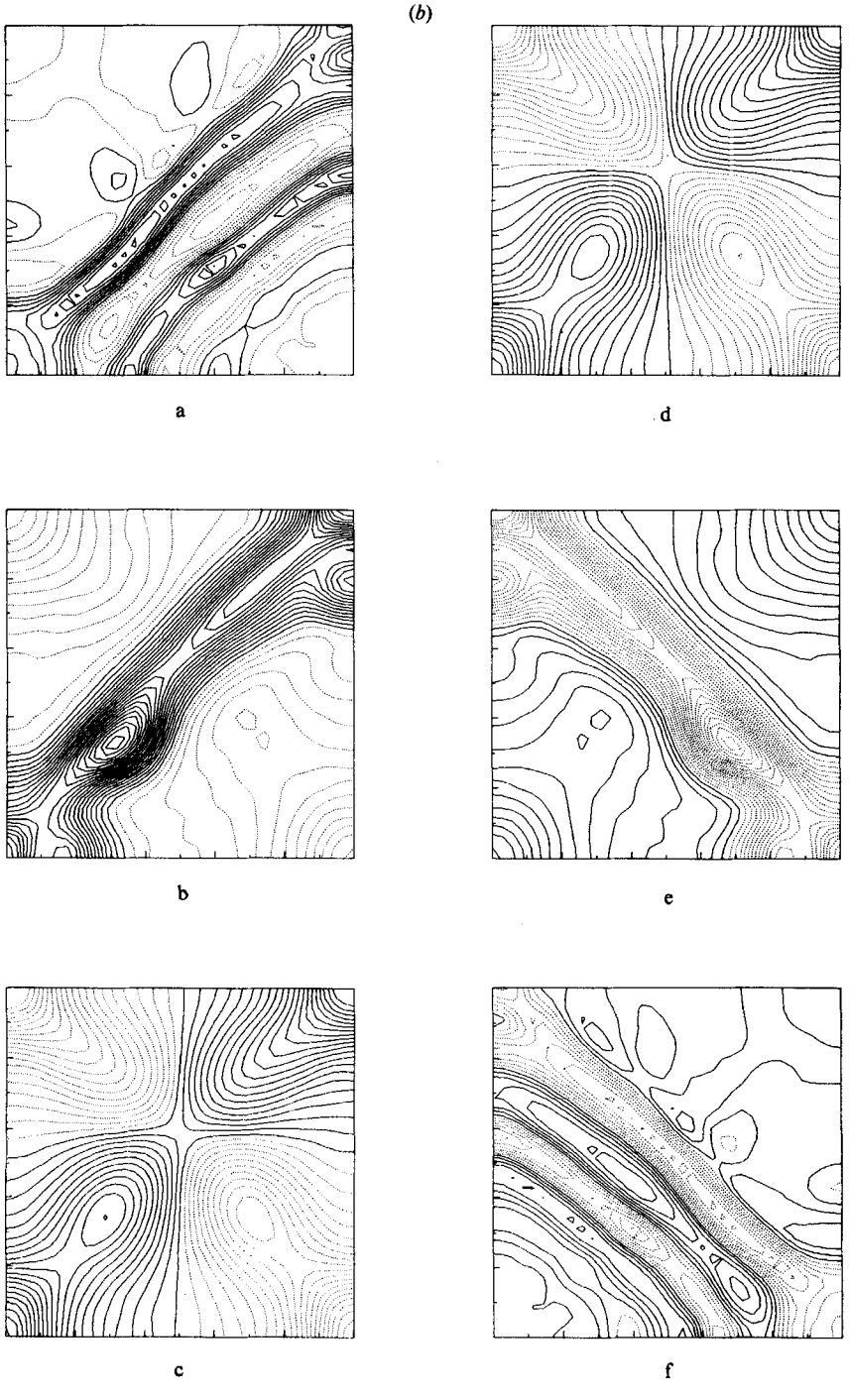

FIGURE 15(*b*). For caption see page 184.

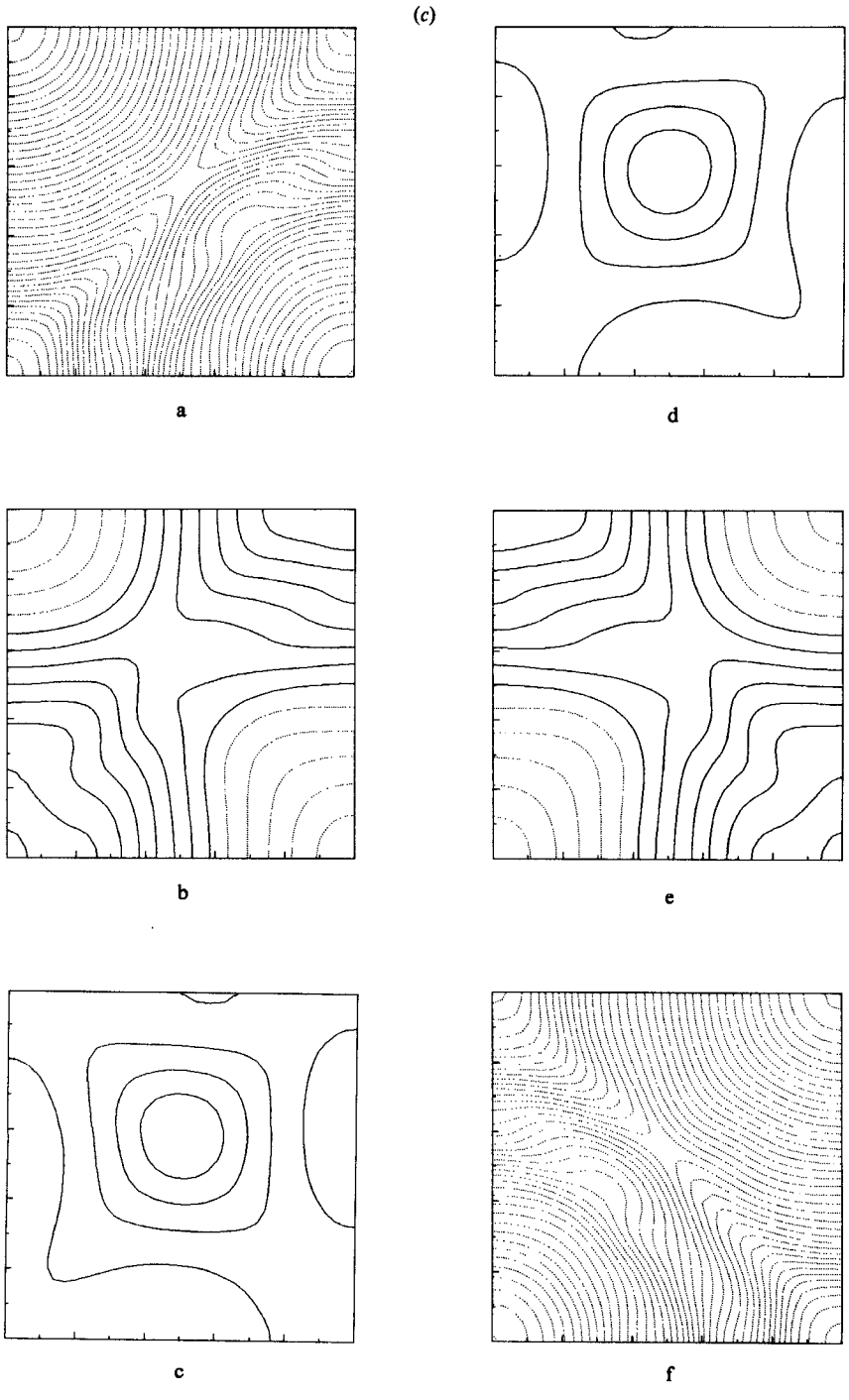

FIGURE 15. Contours of (*a*) θ, (*b*) w, and (*c*) ϕ_ζ at each horizontal cut at $R = 740$ ($N = 34$). The intervals of θ and w are 0.05 and 10 respectively; the intervals of ϕ_ζ are 1 for b–e and 2 for a and f.

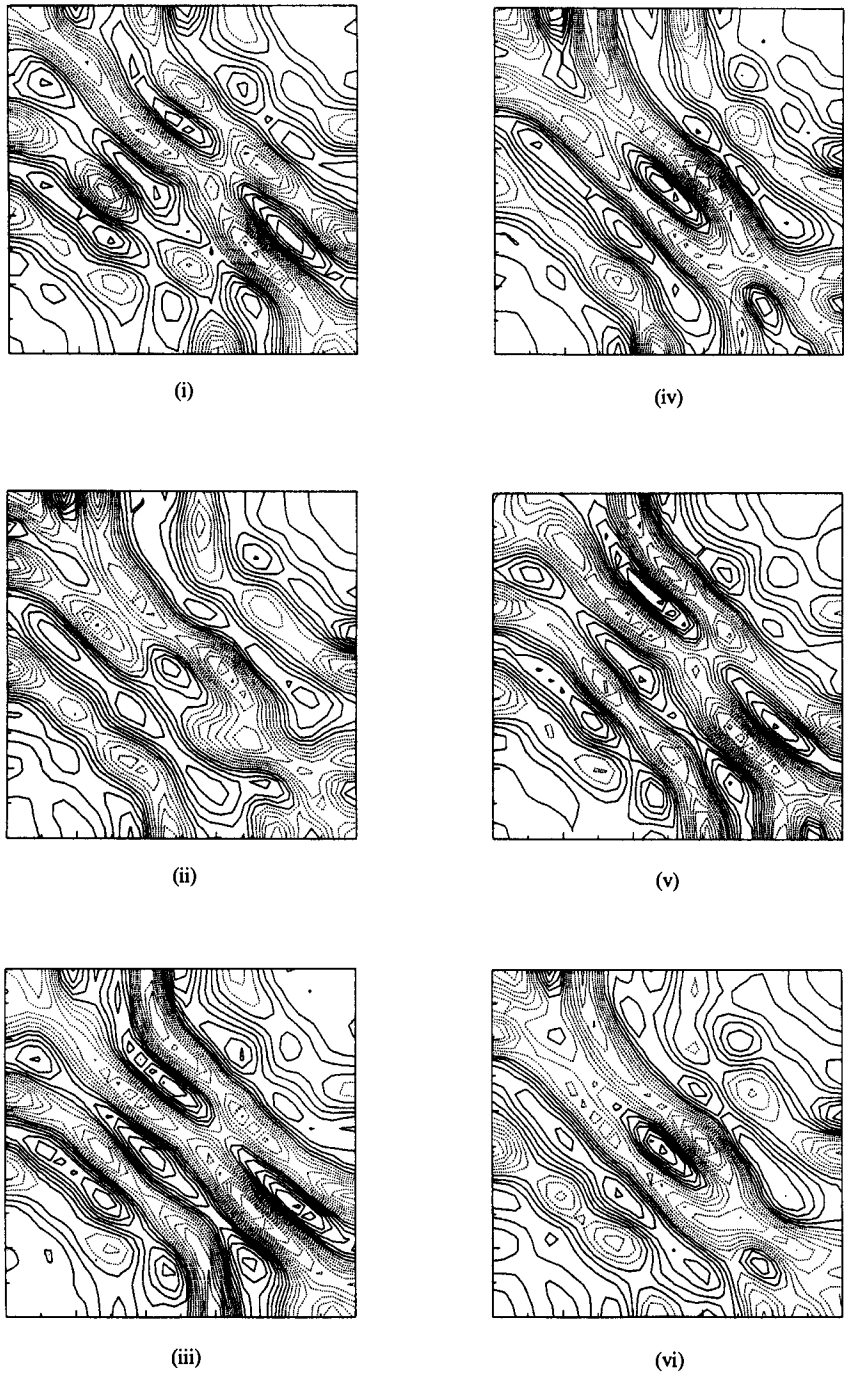

FIGURE 16. Contours of w in the horizontal cut at the vertical position of f when $R = 740$ and $N = 30$. The interval of the contours is 10. Plates (i)–(vi) show flows at six consecutive times; the time interval is 0.0017.

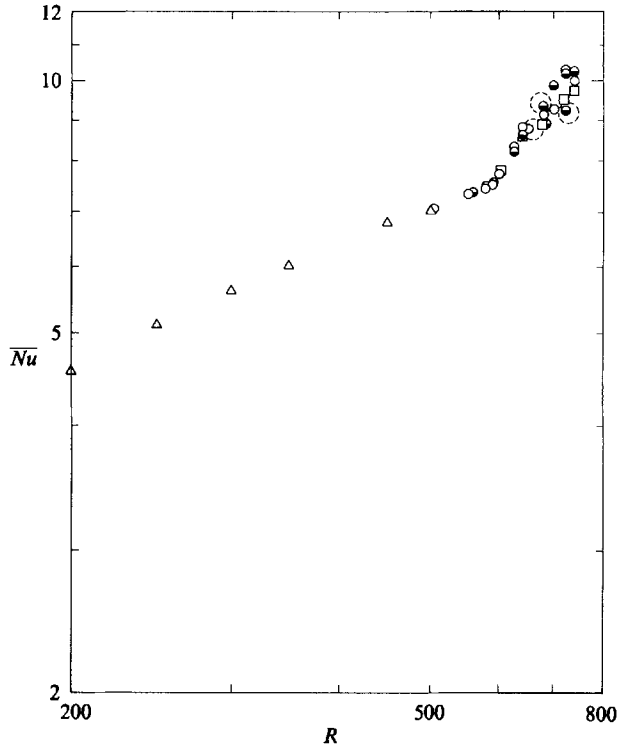

FIGURE 17. Nusselt number as a function of R. Time-averaged values are plotted in oscillatory convection. △, data generated with $N = 20$, and other symbols are all defined in figures 11 and 12.

There have been two suggestions for the mechanism of oscillation. One is the gravitional instability of thermal boundary layers, which is often attributed to Howard (1964). The other involves advection of periodically pinched-off thermal blobs along the top and bottom walls (Moore & Weiss 1973). The present numerical calculations support the mechanism proposed by Howard, since no isolated thermals were detected in the contour diagrams (plates b–e in figure 9*a* and figure 15*a*). The observation is consistent with our earlier work on two-dimensional single-cell convection and with recent work of Steen & Aidun (1988).

3.5. *Time-averaged Nusselt number*

The $\overline{Nu}$–R relation for R up to 500 reported by Schubert & Straus (1979) was based on solutions obtained with relatively low truncation numbers and symmetry restrictions. We summarize the heat transport results obtained by the present numerical simulations in figure 17. For $R = 200$, 250 and 300 our results agree well with those reported by Schubert & Straus (1979). For example, at $R = 200$ they give $Nu = 5.104$ with $N = 12$, while our computation yields $Nu = 5.144$ with $N = 20$. In the range $200 < R < 575$ (the critical Rayleigh number for the onset of oscillation) $\overline{Nu} \propto R^{0.44}$ is a good fit to the numerically generated data. Within the Rayleigh-number range of the $P^{(1)}$ states, the slope of the $\overline{Nu}$–R relation becomes much steeper than the trend in the steady-state regime. However, once the $QP^{(1)}$ state sets in, because of intermittency, the time-averaged Nusselt number varies often by 10%, depending on respective oscillatory states. The data in figure 17 corresponding to different oscillatory states are shown with dashed circles. Despite these relatively scattered

data, the $\overline{Nu}$–R power-law relation in the QP state is consistent with the one in the $P^{(1)}$ state, and the trend is in good agreement with $\overline{Nu} \propto R^{1.2}$, significantly steeper than the steady-state trend. The Nusselt number of three-dimensional convection in a cube exceeds that of two-dimensional convection in a square by 10–20% for the Rayleigh-number range studied here ($200 < R < 740$).

4. Concluding remarks

We have carried out numerical calculations to determine the evolution with R of the (1, 1, 1) mode of convection in a cubical enclosure filled with a saturated porous medium. We used an efficient numerical code based on the pseudospectral method. No symmetry restrictions were imposed *a priori* on the spectral coefficients. This enabled us to study the general properties of three-dimensional convection. We found both similarities and differences between the two-dimensional mode (1, 0, 1) and the fully three-dimensional mode. The presence of oscillatory convection at sufficiently high Rayleigh numbers, the appearance of a simply periodic regime at the onset of oscillation, and the occurrence of a transition from more complex to less complex flows are common features of two- and three-dimensional convection. On the other hand, there are quantitative differences between two- and three-dimensional convection and a number of characteristics are unique to the three-dimensional (1, 1, 1) convective mode. Both the critical Rayleigh number for the onset of oscillation and the onset frequency are higher for the three-dimensional case: $R = 575$ and $f = 175$ for the (1, 1, 1) mode, while $R = 390$ and $f = 82.5$ for the (1, 0, 1) mode. Partial symmetry breaking, the $S \rightarrow S'$ transition, precedes the onset of oscillatory convection in three-dimensional flow, though the dependence of this transition on the step size in R raises some doubt regarding the validity of this conclusion. The quasi-periodic state of three-dimensional convection exhibits intermittency, each regime differing in spectral characteristics, variance and average Nusselt number, indicating that the flows in the quasi-periodic state are very sensitive to outer disturbances. The Nusselt number (the time-averaged Nusselt number in time-dependent flows) of the three-dimensional flows is generally greater than that of the two-dimensional flows.

Symmetry in the ζ-direction (antisymmetry with respect to $\zeta = 0.5$ and a 90° rotation about the axis of $\xi = \eta = 0.5$) are still present at $R = 740$, the highest Rayleigh number in the present study. However, the gradual growth of coefficients which violate this symmetry was observed, and it is possible that eventual symmetry breaking in the ζ-direction could trigger the transition to chaotic flow at a higher Rayleigh number, just as in the two-dimensional case. Effects of symmetry constraints on the evolution with R of convection are therefore significant, as has been also pointed out by McLaughlin & Orszag (1982) and Kessler (1987). The truncation number was again found to be a crucial parameter in the quantitative identification of the nature of time-dependent convection. We used the high truncation numbers $N = 20$, 26, 30 and 34 to ensure the validity of the time-dependent results.

We would like to acknowledge support from the National Science Foundation (Grant MEA 82-18600), the University of California, and the Agency of Industrial Science and Technology in the Ministry of International Trade and Industry, which provided computing time on the IBM308IK through the Research Information Processing System. Our appreciation must also be extended to Mr Y. Saito, who has carried out a number of numerical calculations.

REFERENCES

AIDUN, C. K. & STEEN, P. H. 1986 Transition to oscillatory convective heat transfer in fluid-saturated porous medium. *AIAA/ASME 4th Joint Thermophysics and Heat Transfer Conf., AIAA paper* 86–1264.

AIDUN, C. K. & STEEN, P. H. 1987 Transition to oscillatory heat transfer in a fluid-saturated porous medium. *J. Thermophys.* **1**, 268–273.

BECK, J. L. 1972 Convection in a box of porous material saturated with fluid. *Phys. Fluids* **15**, 1377–1383.

CALTAGIRONE, J. P. 1975 Thermoconvective instabilities in horizontal porous layers. *J. Fluid Mech.* **72**, 269–287.

GARY, J. & KASSOY, D. R. 1981 Computation of steady and oscillatory convection in saturated porous media. *J. Comput. Phys.* **40**, 120–142.

GARY, J., KASSOY, D. R., TRADJERAN, H. & ZEBIB, A. 1982 The effects of significant viscosity variation on convective heat transfer in water-saturated porous media. *J. Fluid Mech.* **117**, 233–249.

GOLLUB, J. P. & BENSON, S. V. 1980 Many routes to turbulent convection. *J. Fluid Mech.* **100**, 449–470.

GOTTLEIB, D. & ORSZAG, S. A. 1977 *Numerical Analysis of Spectral Methods: Theory and Applications.* SIAM.

HOLST, P. H. & AZIZ, K. 1972 Transient three-dimensional natural convection motion in a confined porous medium. *Intl. J. Heat Mass Transfer* **15**, 73–90.

HORNE, R. N. 1979 Three-dimensional natural convection motion in a confined porous medium heated from below. *J. Fluid Mech.* **92**, 751–766.

HORNE, R. N. & CALTAGIRONE, J. P. 1980 On the evolution of thermal disturbances during natural convection in a porous medium. *J. Fluid Mech.* **100**, 385–395.

HORNE, R. N. & O'SULLIVAN, M. J. 1974 Oscillatory convection in a porous medium heated from below. *J. Fluid Mech.* **66**, 339–352.

HOWARD, L. N. 1964 Convection at high Rayleigh number. In *Proc. 11th Intl Congr. Appl. Mech., Munich,* pp. 1109–1115. Springer.

KESSLER, R. 1987 Nonlinear transition in three-dimensional convection. *J. Fluid Mech.* **174**, 357–379.

KIMURA, S., SCHUBERT, G. & STRAUS, J. M. 1986 Route to chaos in porous-medium thermal convection. *J. Fluid Mech.* **116**, 305–324.

KIMURA, S., SCHUBERT, G. & STRAUS, J. M. 1987 Instabilities of steady, periodic, and quasi-periodic modes of convection in porous media. *Trans. ASME* C: *J. Heat Transfer* **109**, 350–335.

KOSTER, J. N. & MÜLLER, V. 1984 Oscillatory convection in vertical slots. *J. Fluid Mech.* **139**, 363–390.

MACLAUGHLIN, J. B. & ORSZAG, S. A. 1982 Transition from periodic to chaotic thermal convection. *J. Fluid Mech.* **122**, 123–142.

MARCUS, P. S. 1981 Effects of truncation in model representations of thermal convection. *J. Fluid Mech.* **103**, 241–255.

MOORE, D. R. & WEISS, N. O. 1973 Two-dimensional Rayleigh–Bénard convection. *J. Fluid Mech.* **58**, 289–312.

ORSZAG, S. A. 1971 Numerical simulation of incompressible flows within simple boundaries. *Stud. Appl Maths* **50**, 293–327.

SCHUBERT, G. & STRAUS, J. M. 1979 Three-dimensional and multi-cellular steady and unsteady convection in fluid-saturated porous media at high Rayleigh numbers. *J. Fluid Mech.* **94**, 25–36.

SCHUBERT, G. & STRAUS, J. M. 1982 Transitions in time-dependent thermal convection in fluid-saturated porous media. *J. Fluid Mech.* **121**, 301–313.

STEEN, P. H. 1983 Pattern selection for finite amplitude convection states in boxes of porous media. *J. Fluid Mech.* **136**, 219–242.

STEEN, P. H. & AIDUN, C. K. 1988 Time-periodic convection in porous media: transition mechanism. *J. Fluid Mech.* **196**, 263–290.

STRAUS, J. M. 1974 Large amplitude convection in porous media. *J. Fluid Mech.* **64**, 51–63.

STRAUS, J. M. & SCHUBERT, G. 1979 Three-dimensional convection in a cubic box of fluid-saturated porous material. *J. Fluid Mech.* **91**, 155–165.

ZEBIB, A. & KASSOY, D. R. 1978 Three-dimensional natural convection motion in a confined porous medium. *Phys. Fluids* **21**, 1–3.